



Rotation of Low-mass Stars in Upper Centaurus–Lupus and Lower Centaurus–Crux with TESS

L. M. Rebull¹ , J. R. Stauffer² , L. A. Hillenbrand³, A. M. Cody⁴ , Ethan Kruse⁵ , and Brian P. Powell⁵ ¹ Infrared Science Archive (IRSA), IPAC, 1200 E. California Blvd., California Institute of Technology, Pasadena, CA 91125, USA; rebull@ipac.caltech.edu² Spitzer Science Center (SSC), IPAC, 1200 E. California Blvd., California Institute of Technology, Pasadena, CA 91125, USA³ Astronomy Department, California Institute of Technology, Pasadena, CA 91125, USA⁴ SETI Institute, 189 Bernardo Avenue, Suite 200, Mountain View, CA 94043, USA⁵ NASA Goddard Space Flight Center, Greenbelt, MD 20771, USA

Received 2022 April 19; revised 2022 May 24; accepted 2022 May 25; published 2022 August 3

Abstract

We present stellar rotation rates derived from Transiting Exoplanet Survey Satellite (TESS) light curves for stars in Upper Centaurus–Lupus (UCL; ~ 136 pc, ~ 16 Myr) and Lower Centaurus–Crux (LCC; ~ 115 pc, ~ 17 Myr). We find spot-modulated periods (P) for $\sim 90\%$ of members. The range of light-curve and periodogram shapes echoes that found for other clusters with K2, but fewer multiperiod stars may be an indication of the different noise characteristics of TESS, or a result of the source selection methods here. The distribution of P as a function of color as a proxy for mass fits nicely in between that for both older and younger clusters observed by K2, with fast rotators being found among both the highest and lowest masses probed here, and a well-organized distribution of M-star rotation rates. About 13% of the stars have an infrared excess, suggesting a circumstellar disk; this is well matched to expectations, given the age of the stars. There is an obvious pileup of disked M stars at $P \sim 2$ days, and the pileup may move to shorter P as the mass decreases. There is also a strong concentration of disk-free M stars at $P \sim 2$ days, hinting that perhaps these stars have recently freed themselves from their disks. Exploring the rotation rates of stars in UCL/LCC has the potential to help us understand the beginning of the end of the influence of disks on rotation, and the timescale on which stars respond to unlocking.

Unified Astronomy Thesaurus concepts: [Stellar rotation \(1629\)](#); [Stellar associations \(1582\)](#); [Low mass stars \(2050\)](#)

Supporting material: machine-readable tables

1. Introduction

The Scorpius–Centaurus OB Association is the closest association to the Sun including massive star formation, and, as such, it is both important for our studies of young stars and difficult to study in its entirety, because it subtends large angles on the sky, more than 4700 square degrees. In the context of Hipparcos results, de Zeeuw et al. (1999) summarized the literature, starting with Kapteyn (1914). Blaauw (1964) broke Scorpius–Centaurus into three subgroups, namely Upper Scorpius or Upper Sco (USco), Upper Centaurus–Lupus (UCL), and Lower Centaurus–Crux (LCC). de Zeeuw et al. (1999) defined boundaries in Galactic coordinates (see Figure 1) for USco ($l \sim 343^\circ - 360^\circ$, $b \sim 10^\circ - 30^\circ$), LCC ($l \sim 285^\circ - 312^\circ$, $b \sim -10^\circ - 21^\circ$), and UCL ($l \sim 312^\circ - 350^\circ$, $b \sim 0^\circ - 25^\circ$; with a “bite” taken out of it to allow for USco).⁶ It has been difficult to identify members of these groups not only because they cover a large swath of sky, but also because this region is in the Galactic plane and close to the Galactic center, so there is a high surface density of nonmember (NM) stars.

In recent years, all-sky surveys, as well as instruments that can quickly cover large areas of sky, have enabled more complete catalogs of members. Gaia (Gaia Collaboration et al.

2016b, 2018a), in particular, has greatly expanded our knowledge of these clusters. Many groups have recently used Gaia Data Release 2 (DR2; Gaia Collaboration et al. 2018b) to select USco/UCL/LCC members (e.g., Goldman et al. 2018; Zari et al. 2018; Damiani et al. 2019; Kounkel & Covey 2019; Kerr et al. 2021, and references therein). There are known age and distance differences among the three subgroups—USco is at ~ 143 pc and ~ 11 Myr, UCL is at ~ 136 pc and ~ 16 Myr, and LCC is at ~ 115 pc and ~ 17 Myr (see Wright & Mamajek 2018 for distances and Pecalet et al. 2012 for ages, though the ages are still controversial and USco may be as young as 3 Myr—see Rebull et al. 2018 and references therein). We have taken USco here to be ~ 8 Myr, based on David et al. (2019). There is likely additional substructure within these three broad groupings (see, e.g., Damiani et al. 2019 or Kerr et al. 2021, and references therein), although, in the context of this paper, we have limited the groups under consideration to UCL and LCC (and USco from our earlier work).

We have recently been working to understand how the rotational evolution of low-mass stars changes as a function of both age and mass. K2 (Howell et al. 2014) revolutionized our understanding of this. We have published thousands of K2 rotation rates from the Pleiades (~ 125 Myr; Rebull et al. 2016a, 2016b; Stauffer et al. 2016; Papers I, II, and III, respectively), Praesepe (~ 790 Myr; Rebull et al. 2017; Paper IV), USco/ ρ Oph (~ 8 Myr and ~ 1 Myr, respectively; Rebull et al. 2018; Paper V), and Taurus/Taurus Foreground (~ 3 – 5 Myr and ~ 30 Myr, respectively; Rebull et al. 2020, 2021; Paper VI). Others have also published legions of stellar rotation

⁶ No points belonging to UCL are “hidden” under the USco box in Figure 1; the vertices of the UCL box are (all in l , b , in degrees): 350, 0; 312, 0; 312, 25; 343, 25; 343, 10; 350, 10; and 350, 0.

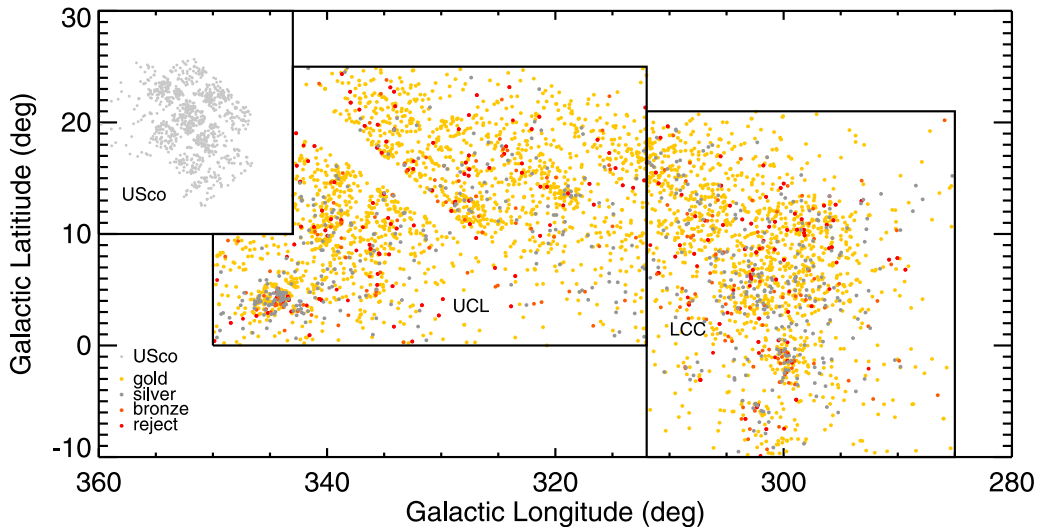


Figure 1. The locations of the targets in Galactic coordinates. The black lines denote the classical boundaries between USco, UCL, and LCC according to de Zeeuw et al. (1999); see the text. Note that no points belonging to UCL are “hidden” under the USco box. The gold, silver, and bronze members (see Section 2.3) are indicated, along with the rejected (discarded) sources (red). The gaps in the spatial distribution are an artifact of the TESS observation strategy. The targets from USco with rotation periods (Paper V) are shown in light gray, in the upper left; gaps between the K2 chips are readily apparent. Note that these regions are in the Galactic plane and near the Galactic center, and, as a result, given the large pixel size in TESS, source confusion is a concern. Note also that the UCL/LCC member sample is overwhelmingly gold ($\sim 80\%$).

rates, using Kepler and K2 (e.g., Curtis et al. 2020; Popinchalk et al. 2021; Rampalli et al. 2021, and references therein).

Disk lifetimes are mass-dependent (and wavelength-dependent), but are likely between ~ 2 and ~ 20 Myr (see, e.g., Ribas et al. 2014, 2015), with longer-lived disks around lower-massed stars. USco has a disk fraction of $\sim 10\%$ – 25% (see, e.g., Luhman & Mamajek 2012), whereas UCL/LCC has a disk fraction of a few percent (see, e.g., Goldman et al. 2018). Exploring the rotation rates of the stars in UCL/LCC has the potential to help us understand the beginning of the end of the influence of disks on rotation, and the timescale on which the star responds to unlocking. Since there have been several recent papers identifying many thousands of members of UCL/LCC, and since NASA’s Transiting Exoplanet Survey Satellite (TESS; Ricker et al. 2015) is surveying the whole sky for variability, now is an opportune time to explore the rotation rates of low-mass stars in UCL/LCC to see how they fit in with the rotation rates that are already known.

We have deliberately performed our analyses of all of our space-based light curves (LCs) and supporting data for stars in all of these clusters, now including UCL/LCC, in as homogeneous a fashion as possible, in order to best compare the rotation data across these clusters.

In preparation for discussing the distribution of the rotation rates in UCL/LCC, we start by assembling the sample of member stars and defining the member subsamples that we use throughout the rest of the paper in Section 2. The initial sample is constructed from several papers presenting members, which we then winnow into four sets of targets: gold (the vast majority of the member sample in the end, $\sim 80\%$), silver, and bronze members, and rejected (discarded) targets. These sets are highlighted in tables and figures throughout the paper; the gold sample is the best possible sample, and all the periods (P) measured for these stars are high confidence. Section 3 describes in more detail all the supporting data amassed to enable this analysis, and Section 4 describes the TESS data, how we deal with confusion and contamination, and how we

find and interpret periods in the LCs. Section 5 considers the UCL/LCC sample as a whole, and the member subsamples within it. Section 6 presents the distribution of the periods with color as a proxy for mass for UCL/LCC in context with other clusters, including specifically considering the stars with disks. Finally, we summarize in Section 7. There are several Appendices on rejected stars, literature periods, unusual LCs, and timescales.

2. Sample Definition

We start with a set of literature members (Section 2.1) and, in the end (Section 2.3), have four sets of targets, which are assembled based on membership confidence and the reliability of the linkage between the LC and the star in question: gold (the vast majority of the member sample, $\sim 80\%$), silver, bronze, and rejected (discarded) targets. The gold members have K_s photometry (and either V measured explicitly or an inferred ($V - K_s$)), distances (Bailer-Jones et al. 2018) in the right regime (< 300 pc), and no indications of source confusion in their TESS LC (see the discussion below in Section 4.2). (It also turns out that the periodic gold members all have highly reliable periods, though that was not imposed upon the sample.) The silver members have each got all of the relevant photometry and only one reason to be concerned about them, which could be a distance that may be too far (see Section 3.5) or a suggestion that the LC might be contaminated (see Section 4.2). The bronze members have all relevant photometry and two reasons to be concerned. Targets that have three or more reasons to be concerned, or that are obviously subject to source confusion, are rejected.

Because we will be referring to these subsamples throughout the paper, we also take the opportunity here to start to put the sample in context (Section 2.2) and present all the statistics in one place—see Table 1 for the numbers of stars and sample fractions.

Table 1
Summary of the Statistics of the UCL/LCC Sample^a

| Property | Initial Literature | All TESS Sources | Gold Members | Silver Members | Bronze Members | All Members | NM or Rejected Sources |
|------------------------------------|--------------------|------------------|--------------|----------------|----------------|-------------|------------------------|
| Count | 5264 | 4101 | 2978 | 542 | 194 | 3714 | 387 |
| Listed in Zari et al. (2018) | 3170 (0.60) | 2715 (0.66) | 2007 (0.67) | 335 (0.62) | 124 (0.64) | 2466 (0.66) | 249 (0.64) |
| Listed in Damiani et al. (2019) | 3887 (0.74) | 2895 (0.71) | 2025 (0.68) | 428 (0.79) | 152 (0.78) | 2605 (0.70) | 290 (0.75) |
| Listed in Pecauc & Mamajek (2016) | 391 (0.10) | 351 (0.09) | 289 (0.10) | 16 (0.03) | 7 (0.04) | 312 (0.08) | 39 (0.10) |
| Has eleanor LC | | 3627 (0.88) | 2646 (0.89) | 437 (0.81) | 180 (0.93) | 3263 (0.88) | 364 (0.94) |
| Has CDIPS LC | | 3384 (0.83) | 2477 (0.83) | 437 (0.81) | 160 (0.82) | 3074 (0.83) | 310 (0.80) |
| Has QLP LC | | 2173 (0.53) | 1683 (0.57) | 201 (0.37) | 69 (0.36) | 1953 (0.53) | 220 (0.57) |
| Used eleanor LC as best | | 2533 (0.62) | 1789 (0.60) | 329 (0.61) | 135 (0.70) | 2253 (0.61) | 280 (0.72) |
| Used CDIPS LC as best | | 1287 (0.31) | 976 (0.33) | 180 (0.33) | 45 (0.23) | 1201 (0.32) | 86 (0.22) |
| Used QLP LC as best | | 281 (0.07) | 213 (0.07) | 33 (0.06) | 14 (0.07) | 260 (0.07) | 21 (0.05) |
| V and K_s measured | | 2934 (0.72) | 2249 (0.76) | 334 (0.62) | 118 (0.61) | 2701 (0.73) | 233 (0.60) |
| $(V - K_s)$ via Gaia DR1 $G - K_s$ | | 241 (0.06) | 185 (0.06) | 29 (0.05) | 14 (0.07) | 228 (0.06) | 13 (0.03) |
| $(V - K_s)$ via Gaia DR2 $G - K_s$ | | 430 (0.10) | 242 (0.08) | 105 (0.19) | 29 (0.15) | 376 (0.10) | 54 (0.14) |
| SED-interpolated V | | 468 (0.11) | 302 (0.10) | 74 (0.14) | 33 (0.17) | 409 (0.11) | 59 (0.15) |
| A_V from JHK_s | | 1657 (0.40) | 1176 (0.39) | 255 (0.47) | 78 (0.40) | 1509 (0.41) | 148 (0.38) |
| A_V from SpTy | | 97 (0.02) | 76 (0.03) | 3 (0.01) | 1 (0.01) | 80 (0.02) | 17 (0.04) |
| Median A_V taken | | 2318 (0.57) | 1726 (0.58) | 284 (0.52) | 115 (0.59) | 2125 (0.57) | 193 (0.50) |
| Has detected IRAC-1 | | 299 (0.07) | 190 (0.06) | 62 (0.11) | 18 (0.09) | 270 (0.07) | 29 (0.07) |
| Has detected WISE-1 | | 3904 (0.95) | 2940 (0.99) | 500 (0.92) | 177 (0.91) | 3617 (0.97) | 287 (0.74) |
| Has detected WISE-3 | | 3742 (0.91) | 2846 (0.96) | 458 (0.85) | 161 (0.83) | 3465 (0.93) | 277 (0.72) |
| Has detected WISE-4 | | 1146 (0.28) | 873 (0.29) | 109 (0.20) | 44 (0.23) | 1026 (0.28) | 120 (0.31) |
| Has clear IR excess | | 354 (0.09) | 242 (0.08) | 61 (0.11) | 20(0.10) | 323 (0.09) | 31 (0.08) |
| Has possible IR excess | | 189 (0.05) | 135 (0.05) | 26 (0.05) | 12 (0.06) | 173 (0.05) | 16 (0.04) |
| Has any IR excess | | 543 (0.13) | 377 (0.13) | 87 (0.16) | 32 (0.16) | 496 (0.13) | 47 (0.12) |
| Obvious source confusion | | 367 (0.09) | 0 (0.00) | 0 (0.00) | 0 (0.00) | 0 (0.00) | 367 (0.95) |
| Distance > 300 pc | | 128 (0.03) | 0 (0.00) | 85 (0.16) | 25 (0.13) | 110 (0.03) | 18 (0.05) |
| TIC contamination > 1.6 | | 434 (0.11) | 0 (0.00) | 160 (0.30) | 178 (0.92) | 338 (0.09) | 96 (0.25) |
| Mean flux suggests contamination | | 589 (0.14) | 0 (0.00) | 290 (0.54) | 185 (0.95) | 475 (0.13) | 114 (0.29) |
| Periodic | | 3640 (0.89) | 2693 (0.90) | 440 (0.81) | 145 (0.75) | 3278 (0.88) | 362 (0.94) |
| Single P | | 555 (0.14) | 2326 (0.78) | 364 (0.67) | 126 (0.65) | 2816 (0.76) | 269 (0.70) |
| Multiple P | | 555 (0.14) | 367 (0.12) | 76 (0.14) | 19 (0.10) | 462 (0.12) | 93 (0.24) |
| Periodic+clear IRx | | 299 (0.07) | 204 (0.07) | 51 (0.09) | 15 (0.08) | 270 (0.07) | 29 (0.07) |
| Multiperiodic+clear IRx | | 42 (0.01) | 28 (0.01) | 7 (0.01) | 1 (0.01) | 36 (0.01) | 6 (0.02) |
| Burster | | 2 (0.00) | 2 (0.00) | 0 (0.00) | 0 (0.00) | 2 (0.00) | 0 (0.00) |
| Dipper | | 56 (0.01) | 39 (0.01) | 7 (0.01) | 0 (0.00) | 46 (0.01) | 10 (0.03) |
| Dipper+clear IRx | | 49 (0.01) | 39 (0.01) | 5 (0.01) | 0 (0.00) | 44 (0.01) | 5 (0.01) |
| Dipper+clear IRx+periodic | | 48 (0.01) | 38 (0.01) | 5 (0.01) | 0 (0.00) | 43 (0.01) | 5 (0.01) |
| Double-dip | | 400 (0.10) | 318 (0.11) | 24 (0.04) | 9 (0.05) | 351 (0.09) | 49 (0.13) |
| Moving double-dip | | 28 (0.01) | 20 (0.01) | 0 (0.00) | 2 (0.01) | 22 (0.01) | 6 (0.02) |
| Shapechanger | | 205 (0.05) | 132 (0.04) | 29 (0.05) | 7 (0.04) | 168 (0.05) | 37 (0.10) |
| Scallop/clouds? ^b | | 99 (0.02) | 75 (0.03) | 8 (0.01) | 2 (0.01) | 85 (0.02) | 14 (0.04) |
| Beater | | 95 (0.02) | 60 (0.02) | 4 (0.01) | 1 (0.01) | 65 (0.02) | 30 (0.08) |
| Complex peak | | 15 (0.00) | 10 (0.00) | 3 (0.01) | 1 (0.01) | 14 (0.00) | 1 (0.00) |
| Resolved, close peaks | | 264 (0.06) | 170 (0.06) | 35 (0.06) | 11 (0.06) | 216 (0.06) | 48 (0.12) |
| Resolved, distant peaks | | 364 (0.09) | 231 (0.08) | 54 (0.10) | 14 (0.07) | 299 (0.08) | 65 (0.17) |
| Pulsator | | 12 (0.00) | 6 (0.00) | 5 (0.01) | 1 (0.01) | 12 (0.00) | 0 (0.00) |

Notes.

^a The numbers in the table are the raw numbers of the stars meeting the stated criterion/criteria, followed by the sample fraction within the column in parentheses. For example, 68% of the gold member sample appear as members in Zari et al. (2018), while 69% of the entire member sample appear in Damiani et al. (2019).

^b This category includes the scallop shell, persistent flux dip, and transient flux dip categories; see Papers I–VI and Stauffer et al. (2021).

2.1. Initial List of Candidate Members

As we have done for our K2 papers (Papers I–VI), we start with an expansive, encompassing list (~5300 stars), assembled from the literature as follows.

Because UCL and LCC are relatively nearby, many groups have used Gaia DR2 (Gaia Collaboration et al. 2018a) to select

members (e.g., Goldman et al. 2018; Zari et al. 2018; Damiani et al. 2019; Kounkel & Covey 2019). Pecauc & Mamajek (2016) add higher-mass probable UCL/LCC members. For our analysis, we chose to merge the member lists from Zari et al. (2018), Damiani et al. (2019), and Pecauc & Mamajek (2016) to generate our set of UCL and LCC candidates. Note that these

papers are based largely on Gaia DR2, not Early Data Release 3 (EDR3; Gaia Collaboration et al. 2021). These lists contain many duplicates of each other, but there are also many stars that appear in only one list (see Table 1). For Pecaut & Mamajek (2016), we took all the stars from their tables 7 or 9 that are identified as being part of UCL or LCC; note that the classical boundaries for UCL+LCC from de Zeeuw et al. (1999) were imposed by Pecaut & Mamajek (2016). For Zari et al. (2018), we started with their all-sky pre-main-sequence sample, and took only those within the de Zeeuw et al. (1999) classical UCL+LCC boundaries. Damiani et al. (2019) break the population in this region into several subgroups, including clusters that are not UCL/LCC. We took those tagged by them as “LCC” or “D2b” (part of LCC) and within the classical LCC boundaries as members of LCC; for UCL, we took those tagged “UCL” or “D1” (part of UCL) and within the classical UCL boundaries as members of UCL. While Damiani et al. (2019) explore a region beyond the classical boundaries, their Figure 8 indicates that within these boundaries, we are capturing the overwhelming majority of members. The collection of all of these literature members results in ~ 5300 stars thought to be members of UCL/LCC. We matched this list of stars to numbers from the TESS Input Catalog (TIC; Stassun et al. 2018, 2019). Not all of the stars in this initial member catalog have TIC numbers, and not all of the stars with TIC numbers have TESS LCs (see Section 4). In order for the star to be included in this analysis, however, at a minimum, there must be a TIC number and an LC.

2.2. The Sample in Context

As part of putting this large sample into context, we have included in Table 1 the numbers and sample fractions originating in the three literature membership studies. Note that the sample fractions given in Table 1 refer to the final sample of 4101 sources presented in Section 2.3, as opposed to the ~ 5300 stars described thus far. Figure 1 shows the distribution of our USco stars with rotation periods from K2 observations (Paper V) in context with the targets from the present paper in UCL/LCC. The classical boundaries between USco, UCL, and LCC (de Zeeuw et al. 1999) are shown. Note that these regions are in the Galactic plane and near the Galactic center, and, as a result, source confusion is a concern, especially given the size of the TESS pixels (see Section 4). Additionally, IC 2602 is in the lower right of the box defining LCC, the box defining UCL includes the Lupus clouds, and the USco box includes ρ Oph in the lower center (see, e.g., Figure 8 in Damiani et al. 2019); a few objects from Lupus are incorporated in our member list. Finally, we note that a few of the targets in our list appear in the literature as possible members of TWA, η Cha, ϵ Cha, or USco. There are so many objects that are legitimate members of UCL/LCC that the very few objects that may not be members of UCL/LCC are unlikely to make a significant difference in our analysis.

Figure 2 includes a histogram of K_s (see Section 3.1) for this entire set of ~ 5300 stars, for comparison to the other subsets presented below (see, e.g., Section 4). The literature distribution peaks at $K_s \sim 11$ or 12, which is very roughly M4–M5. The faintest literature sources are $K_s \sim 13$.

2.3. Final Culled Sample

The details of the winnowing of the sample are included later in the paper (Sections 3 and 4), but, in summary, the gold sample is the best possible member sample; there is nothing

that we can see that stands in the way of working with these stars in this analysis. To the best of our ability to determine it, the LC goes with the star that we think it does, the star seems to be a legitimate member of UCL or LCC, and the star has all the relevant supporting data. Periodic gold stars all have periods in which we have high confidence, although this was not imposed upon the gold sample. Of the members, the vast majority ($\sim 80\%$) are gold members. The silver membership sample has targets that can be worked with in this analysis, but there is one reason to be concerned that maybe the star is not the best possible sample; perhaps there is some question as to whether the star is a member based on distance, or whether the LC is uncontaminated, such that it really corresponds to the star that we think it does (see Section 4.2). The bronze sample has targets with two reasons to be concerned. Rejected targets encompass those that have three or more reasons to be concerned, or incontrovertible evidence that, at least at this time, we cannot tie a given LC to that star, or we are missing V or K_s photometry (or an LC), such that it is not possible to include that star in subsequent analysis.

In the remainder of this paper, when we use the term “entire sample,” we mean all of the targets with LCs and $(V - K_s)$. When we use the term “all members,” we mean the gold+silver+bronze samples together.

3. Supporting Data

In this section, we amass supporting data from the literature, including photometry (Section 3.1) and spectral types (Section 3.2). As in our earlier papers, we wish to use $(V - K_s)_0$ as a proxy for mass, and we continue to do that here, largely using the same approach. The main reason why we want to use $(V - K_s)_0$ is to enable comparisons with our other clusters; even though Gaia data are available for essentially the entire UCL/LCC sample, Gaia data are not available for all of the stars in the other clusters in Papers I–VI. We describe how we deredden our photometry (where relevant) in Section 3.3. We identify infrared (IR) excesses that we interpret as circumstellar disks (Section 3.4). Finally, we describe the distances that we used here (Section 3.5).

3.1. Literature and Derived Photometry

Based on the coordinates from Gaia DR2, for each of our target stars, we obtained corresponding near- and mid-IR photometry from 2MASS (Skrutskie et al. 2003, 2006), DENIS (DENIS team 1999; Epchtein et al. 1999), WISE/AllWISE (Wright et al. 2010a, 2010b), CatWISE (CatWISE team 2020; Eisenhardt et al. 2020), unWISE (Meisner et al. 2019; unWISE Team 2019), Spitzer (Werner et al. 2004) SEIP⁷ (Capak 2013), and AKARI (Murakami et al. 2007; AKARI team 2010a, 2010b). We obtained optical broadband photometry from Gaia Data Release 1 (DR1; Gaia Collaboration et al. 2016a, 2016b) and DR2 (Gaia Collaboration et al. 2018a, 2018b), Pan-STARRS DR1 (Chambers et al. 2016), APASS (Henden et al. 2016), NOMAD (Zacharias et al. 2004), the Southern Proper Motion Program (Girard et al. 2011), and the Second-Generation Guide Star Catalog (GSC-II; Lasker et al. 2008). Pecaut & Mamajek (2016) also provide optical magnitudes. We used a typical source matching radius of one arcsecond.

Partly as a check on the source merging across catalogs, we used all of the photometry to generate a spectral energy

⁷ <http://irsa.ipac.caltech.edu/data/SPITZER/Enhanced/SEIP/overview.html>

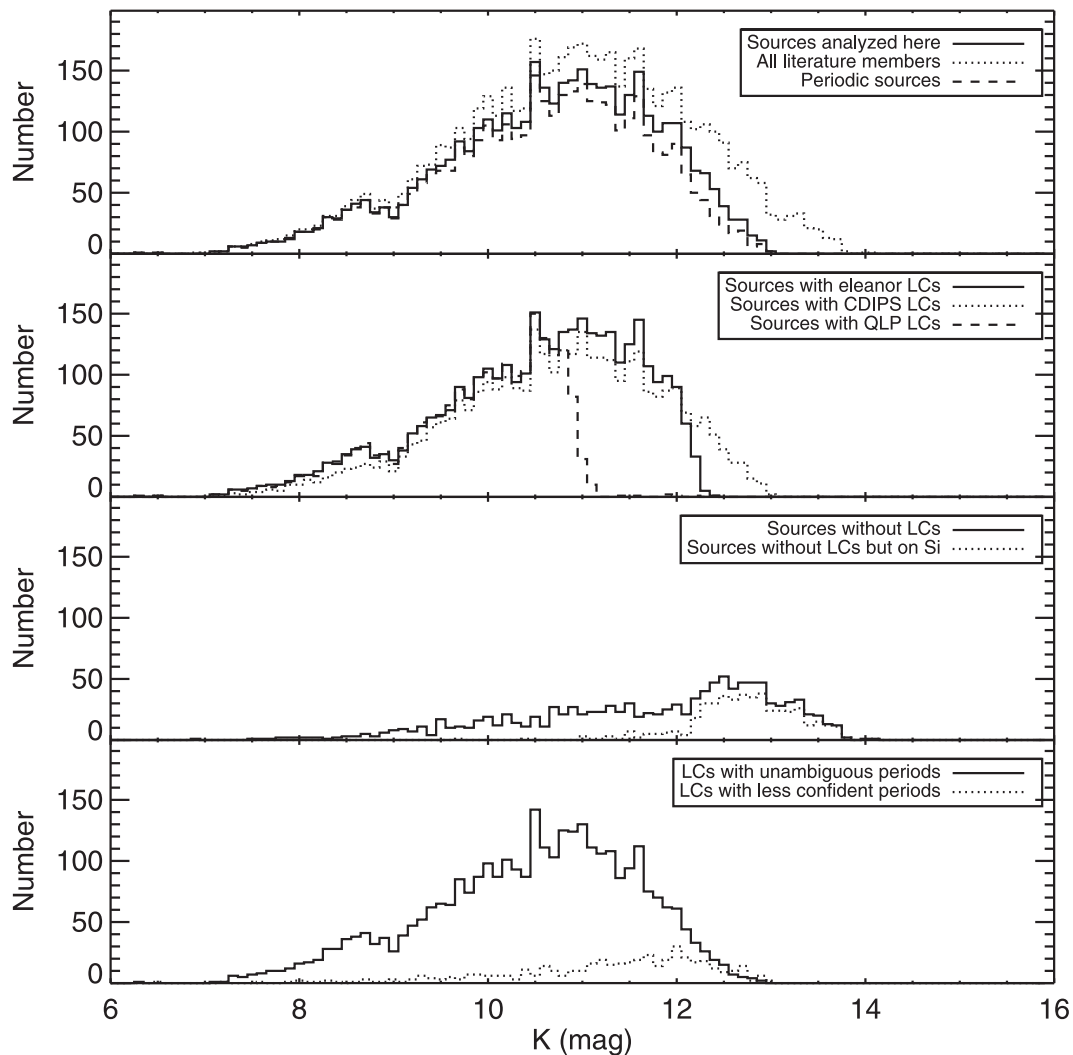


Figure 2. Histograms of the brightness (in K_s) of the targets in the various subsets of data. (Note that the y-axis range is the same in all panels.) Top panel: the sources analyzed here (solid line) in comparison to all the literature sources identified as likely members of UCL/LCC (dotted line) and the sources identified here as periodic (dashed line). The sources that are missing LCs are biased toward fainter sources. Second panel: the sources with *eleanor* LCs (solid line), CDIPS LCs (dotted line), and QLP LCs (dashed line). The QLP LCs are biased toward brighter sources, as expected; the CDIPS LCs can reach fainter magnitudes than the *eleanor* LCs. Third panel: the sources without LCs (solid line) and the sources without LCs that could theoretically exist, as the target was on silicon (“on Si”) during TESS’s first year of operations (dotted line). The targets that are missing LCs are strongly biased toward fainter stars. Fourth panel: the sources with LCs that have unambiguous periods (solid line) and the LCs where the periods are less confident (dotted line). The targets with less confident periods are on average fainter. Based on these histograms, we conclude most importantly that the selection effect imposed by our requirement that there be an LC does not unduly bias our results; we are missing some of the fainter targets, which is unsurprising.

distribution (SED) for each source. If the photometric data from one catalog were obviously inconsistent with the rest of the SED, we removed the data points from that catalog for that source, on the assumption that the positional match failed. We also used the Infrared Science Archive (IRSA) Finder Chart⁸ tool (as well as IRSA Viewer) to investigate such source mismatches.

As part of this process, we investigated the WISE and Spitzer (if relevant) images of the target. The WISE objects that were identified as detections, but did not appear obvious in the image and had detections that were not consistent with the rest of the SED, were changed to be upper limits. If Spitzer data existed and the source was visible, but photometry from SEIP was not available, we performed standard aperture photometry on the SEIP mosaics. About

10% of the entire list of sources was missing photometry and patched in this fashion.

We need $(V - K_s)$ for our target stars, to use as a proxy for mass when comparing to other clusters from our Papers I–VI. Essentially all of the stars in our entire sample have measured K_s (see Figure 2), so we need to find or calculate V . A substantial fraction of the targets have measured V magnitudes in the literature. In cases where V magnitudes were obtainable from more than one place (APASS, NOMAD, GSC-II, and/or Pecaut & Mamajek 2016), we calculated an average V (see Table 1). Other methods that we have used in our other papers ($(V - K_s)$ from Gaia DR1 or V from interpolation of the assembled SED) were necessary for some targets. A few targets missing data from Gaia DR1, but having data in DR2, necessitated the derivation of a new relationship between $(V - K_s)$ and Gaia DR2.⁹ Nearly all

⁸ <https://doi.org/10.26131/IRSA540>

⁹ Where $x = G - K_s$, $V - K_s = -1.383 + 3.554x + (-1.442)x^2 + 0.347x^3 + (-0.026)x^4$. This works well enough for $G - K_s < 5$ and $V - K_s < 7$.

of the targets thus have a measured or inferred ($V - K_s$); see Table 1. However, specifically because we have had to infer ($V - K_s$) values in many cases, this likely contributes scatter to the distribution.

Stars missing K_s or ($V - K_s$) cannot be analyzed in the same way as the rest of the entire sample, so those stars are effectively rejected. Most of those missing K_s are blends with nearby stars, so the TESS LC is certain to be subject to source confusion anyway (see Section 4).

Table 2 includes, for members, the relevant supporting photometric data, including the observed or interpolated ($V - K_s$), and the IR excess assessments (from Section 3.4), plus the periods that we derive (from Section 4). A similar table with all the stars that we had to reject appears in Appendix A.

3.2. Spectral Types

We obtained spectral types from Comerón et al. (2009), Skiff (2014), Galli et al. (2015), Jang-Condell et al. (2015), Mellon et al. (2017), Faherty et al. (2018), Goldman et al. (2018), Nicholson et al. (2018), Bowler et al. (2019), Cruzalèbes et al. (2019), Moolekamp et al. (2019; largely photometric types), and Luhman (2022a, 2022b); finally, if no other types were available, we also consulted SIMBAD¹⁰ for any additional spectral types. In the end, we have spectral types for less than 20% of the member sample. We have few stars with types earlier than G0, and few later than M6.

3.3. Dereddening

Neither UCL nor LCC have substantial or patchy reddening (see, e.g., Pecaut et al. 2012; Mellon et al. 2017). As in our earlier papers, we placed the stars on a $J - H$ versus $H - K_s$ diagram, then shifted them back along the reddening law derived by Indebetouw et al. (2005), to the expected JHK_s colors for young stars from Pecaut & Mamajek (2013) or the T Tauri locus from Meyer et al. (1997), and then converted to $E(V - K_s)$ via $A_K = 0.114A_V$ (Cardelli et al. 1989). Using this approach, nearly 80% of the member sample has essentially no reddening.

Figure 3 shows a JHK_s color-color diagram for the sample, demonstrating that there is not much reddening for most targets, and, for that matter, few optically thick disks in the near-IR (see also Section 3.4). (The figure also shows that all the gold/silver/bronze subsamples are largely similar; we have not preferentially discarded red, or reddened, stars, except for those too faint to have TESS LCs.)

We can also start with the spectral type (Section 3.2) and compare the observed colors to those expected for that type from Pecaut & Mamajek (2013), from which the reddening can be derived. This approach is less effective here in UCL/LCC, because there are so few spectral types known; even among those that are, there is not much reddening, in general, toward these stars.

We determined or assigned a reddening of 0 to more than half the stars; we took the reddening derived from the JHK_s colors in about 40% of the entire sample (see Table 1). The values of ($V - K_s$) are included in Table 2 for the members and in Appendix A for the rejected sources. However, as in our earlier papers, to emphasize the net uncertainty, the “v_{mk0}” column in Table 2 has been rounded to the nearest 0.1 mag.

The values used in the plots here can be recovered by using the $E(V - K_s)$ (“ev-k”) and ($V - K_s$)_{observed} (“vk-used”) columns. Table 2 (and its analogous Table 3 for NMs) includes a two-digit code indicating the origin of the ($V - K_s$) value and the method by which the ($V - K_s$) was dereddened to ($V - K_s$)₀ (see Table 2 or 3 for specific definitions).

3.4. IR Excesses

In the process of SED inspection above (Section 3.1), we determined which stars were likely to have unambiguous IR excesses (and therefore likely circumstellar disks, in the case of young stars), and noted the wavelength at which the IR excess begins. We noted those with obvious IR excesses (“high confidence”) separately from those where an IR excess might be present (“low confidence” or “possible”; Table 2). A high-confidence IR excess might be one where the IR excess is large and detected at more than one wavelength, and/or by more than one instrument; a low-confidence IR excess might be one where the excess is in only one band and where $\chi = (\text{IR color}_{\text{observed}} - \text{IR color}_{\text{expected}}) / (\text{error in IR color})$ is between 3 and 5. Our source inspection process (Section 3.1) ensures that all W3 and W4 detections are secure, so an excess that appears solely at W3 might indeed be real. Just a few percent of the targets have high-confidence IR excesses, and fewer have low-confidence IR excesses (see Table 1). This is consistent with prior determinations of the disk fractions in this region (see, e.g., Goldman et al. 2018). Checking against the literature (e.g., Carpenter et al. 2009; Chen et al. 2014; Mittal et al. 2015; Cotten & Song 2016; Luhman 2022a, 2022b) suggests that our selection mechanism has found the obvious disks, but has indeed missed debris disks with very small IR excesses, which is expected, given our approach. To securely and systematically identify subtle excesses would require spectral types and modeling beyond the scope of the present paper.

The Spitzer data do not cover the whole region, but the WISE data do. WISE detections, even of photospheres, at 12 μm are common at this distance, but 22 μm limits are also common. Detections from other IR surveys at $\geq 5 \mu\text{m}$ are relatively rare. Figure 4 shows the [W1] versus [W1]–[W3] for the stars discussed here. Most of the excesses obvious by eye from this plot are selected as high- or low-confidence excesses. The points that are not identified as disks, but still appear in this plot to have significant [W1]–[W3], are stars for which the only indication of an excess is a marginal [W3] detection with a larger than typical error bar—that is, they do not have a significant excess.

Figure 4 and Table 1 also show that the gold sample has most of the stars with disks (of the stars with unambiguous disks, 68% are in the gold sample); stars with disks are apparently less likely to be at the wrong distance (which makes sense, since young stars in this part of the sky with the right photospheric brightness are more likely than field stars to have IR excesses) or have source confusion issues. We have not preferentially discarded disks; if anything, we seem to have have preferentially retained them.

However, our approach to identifying disks is unambiguously biased toward the sources with large excesses. Many of the sources carefully studied with Spitzer (e.g., Chen et al. 2014) were known well before Gaia to be UCL/LCC members (or simply young), and therefore have many more supporting data in the literature than the more recently identified members. The larger net that we have cast has selected stars that for the most part do not have spectral types (Section 3.2); and, without

¹⁰ <http://simbad.u-strasbg.fr/simbad/>

Table 2
Contents of the Table: Periods and Supporting Data for UCL/LCC Members with Viable LCs

| Number | Column | Contents |
|--------|----------------|---|
| 1 | TIC | Number in the TIC |
| 2 | Name | Coordinate-based (R.A. and decl., J2000) name for target |
| 3 | othername | Alternate name for target |
| 4 | gaiaid | Gaia DR2 ID |
| 5 | distance | Distance from Bailer-Jones et al. (2018) in parsecs |
| 6 | member | Membership sample (gold, silver, or bronze) |
| 7 | Kmag | K_s magnitude (in Vega mags), if observed |
| 8 | vmk-used | $(V - K_s)$ used, in Vega mags (observed or inferred; see text) |
| 9 | evmk | $E(V - K_s)$ adopted for this star (in mags; see Section 3.3) |
| 10 | Kmag0 | Dereddened $K_{s,0}$ magnitude (in Vega mags), as inferred (see Section 3.3) |
| 11 | vmk0 | $(V - K_s)_0$, dereddened $V - K_s$ (in Vega mags), as inferred (see Section 3.3; rounded to nearest 0.1 to emphasize the relatively low accuracy). |
| 12 | r_vmk-used | Source of $(V - K_s)$ (see Section 3.1): 1= V measured directly from the literature (including SIMBAD), and K_s from 2MASS; 2 = V from the literature (see Section 3.1), and K_s from 2MASS; 3= $(V - K_s)$ inferred from Gaia DR1, and G and K_s from 2MASS (see Section 3.1); 4= $(V - K_s)$ inferred from Pan-STARRS1, and G and K_s from 2MASS (see Section 3.1); 6 = V inferred from well-populated optical SED, and K_s from 2MASS (see Section 3.1); 7= $(V - K_s)$ inferred from Gaia DR2, and G and K_s from 2MASS (see Section 3.1); -9 = no measure of $(V - K_s)$. |
| 13 | r_evmk | Source of $E(V - K_s)$ leading to $(V - K_s)_0$ (see Section 3.3): 1=dereddening from JHK_s diagram (see Section 3.3); 2=dereddening back to $(V - K_s)_0$ expected for spectral type; 3=dereddening from SED fits; 4=used median $E(V - K_s)=0$ (see Section 3.3); -9=no measure of $E(V - K_s)$. |
| 14 | P1 | Primary period, in days (taken to be the rotation period in cases where there is >1 period) |
| 15 | P2 | Secondary period, in days |
| 16 | P3 | Tertiary period, in days |
| 17 | P4 | Quaternary period, in days |
| 18 | p-uncertcode | Uncertainty code for period—is there any reason to worry about this period? Values are “n” (no worry, full confidence; by far the most common value), “(n)” (no period), with “n?” and “y?” being progressively less confident periods. |
| 19 | IRexcess | Whether an IR excess is present or not (see Section 3.4) |
| 20 | IRexcessStart | The minimum wavelength at which the IR excess is detected or the limit of our knowledge of where there is no excess (see Section 3.4) |
| 21 | SEDslope | Best-fit slope to all detections between 2 and 25 microns |
| 22 | SEDclass | SED class (I, flat, II, or III), based on the SED slope between 2 and 25 microns |
| 23 | dipper | The LC matches dipper characteristics (see Section 4.5) |
| 24 | burster | The LC matches burster characteristics (see Section 4.5) |
| 25 | single/multi-P | Single or multiperiod star |
| 26 | dd | The LC and power spectrum match double-dip characteristics (see Section 4.5) |
| 27 | ddmoving | The LC and power spectrum match moving double-dip characteristics (see Section 4.5) |
| 28 | shapechanger | The LC matches shape changer characteristics (see Section 4.5) |
| 29 | beater | The LC has beating visible (see Section 4.5) |
| 30 | complexpeak | The power spectrum has a complex, structured peak and/or has a wide peak (see Section 4.5) |
| 31 | resolvedclose | The power spectrum has resolved close peaks (see Section 4.5) |
| 32 | resolveddist | The power spectrum has resolved distant peaks (see Section 4.5) |
| 33 | pulsator | The power spectrum and LC match pulsator characteristics (see Section 4.5) |
| 34 | scallop | The LC matches scallop or flux dip characteristics (see Section 4.5 and Appendix C) |
| 35 | EB | The LC has characteristics of eclipsing binary (see Section 4.5 and Appendix C) |

(This table is available in its entirety in machine-readable form.)

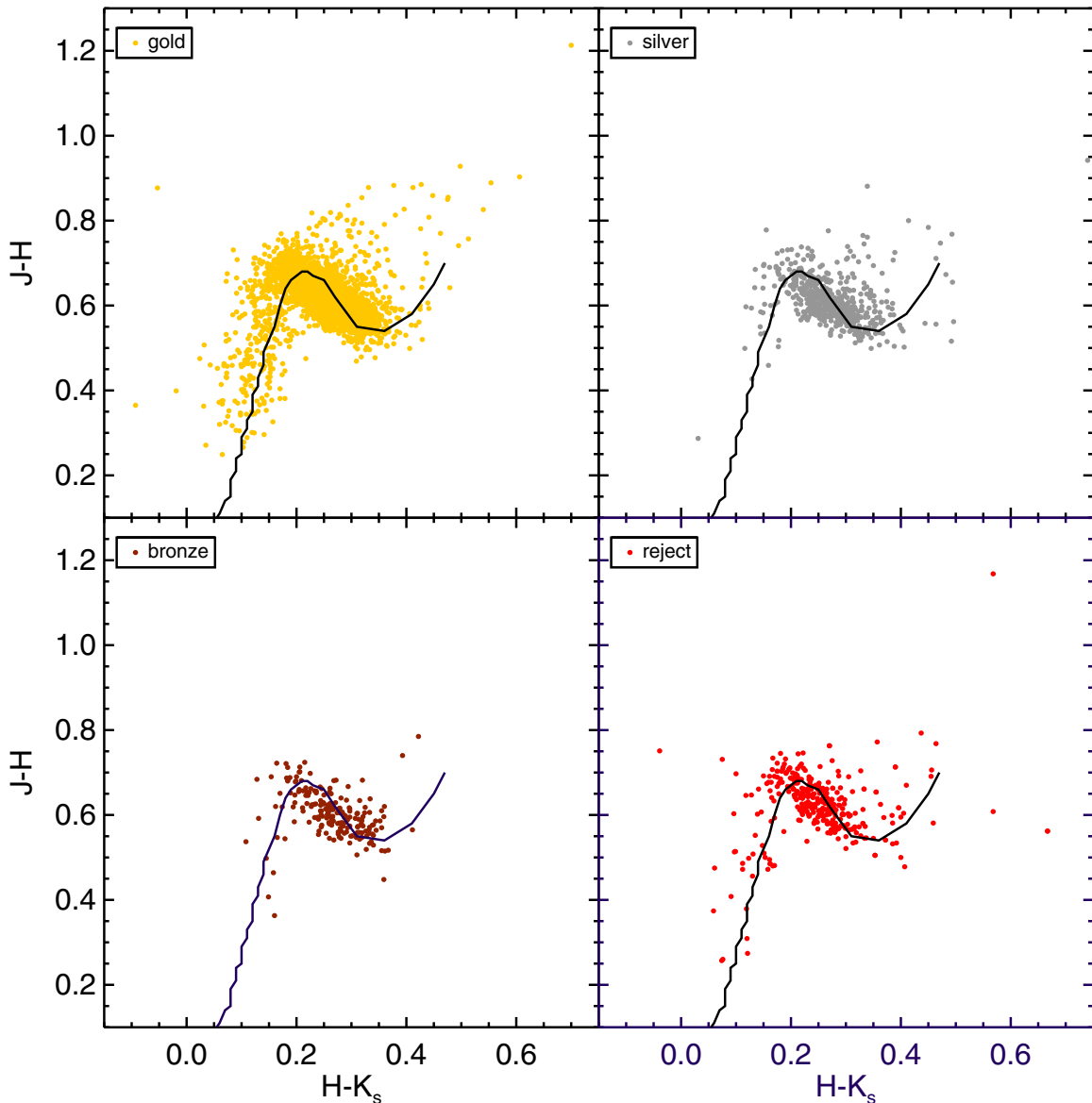


Figure 3. $J - H$ vs. $H - K_s$ (observed) for upper left: gold members (see Section 2.3 for membership); upper right: silver members; lower left: bronze members; and lower right: rejected targets. These plots show that there is not much reddening on average toward these targets (Section 3.3), and, moreover, that the stars that are being dropped are not particularly or obviously different than the ones that are retained.

that constraint in particular, doing careful assessments of small IR excesses is beyond the scope of the present paper.

3.5. Distances

The distances that we used here are those based on Gaia DR2, provided by Bailer-Jones et al. (2018). Since the membership lists that we used as inputs from Zari et al. (2018) and Damiani et al. (2019) both extensively used data from Gaia DR2, we used distances derived from DR2.¹¹ We expected all the members selected in this fashion to have distances appropriate for UCL/LCC, ~ 100 – 200 pc, but for nearly 200 stars the distances retrieved from Bailer-Jones et al. (2018) are >300 pc. These apparently distant sources are not biased toward, say, those members added from Pecaut &

Mamajek (2016), where that analysis was completed pre-Gaia. The distances appear in Table 2 for all members and in Appendix A for the discarded (rejected) sample.

Figure 5 presents histograms of the Bailer-Jones et al. (2018) distances for the entire sample, as well as the gold, silver, and bronze samples, with an indication of how many stars in those three samples have distances >300 pc. All of the gold sample is <300 pc, by definition. A substantial fraction (see Table 1) of the silver sample includes stars that would be in the gold sample, except for their Bailer-Jones et al. (2018) distances. We did not summarily discard these stars, because these stars with >300 pc distances were also identified in the literature from Gaia proper motions as belonging to UCL/LCC (see Section 2.1). All of these Gaia analyses cannot be simultaneously correct. By way of a specific example, a star known to Simbad as Sz 127 (=TIC 255255634) was selected by Zari et al. (2018) as a member of UCL/LCC. It appears in several papers (e.g., Galli et al. 2013) as a member of Lupus, so,

¹¹ Comparing to Bailer-Jones et al. (2021), which uses EDR3, fewer than 40 stars have distances that are significantly different enough from those from Bailer-Jones et al. (2018) that they would be treated differently here.

historically, it has been regarded as quite close to us (less than a kpc). It has an IR excess, which supports its youth. A simple inversion of the Gaia DR2 parallax yields ~ 160 pc; Bailer-Jones et al. (2018) list ~ 1640 pc. Because the distances can be wrong, therefore, if any given star has a Bailer-Jones et al. (2018) distance that places it too far away (>300 pc), then that is just one mark against it, as opposed to a reason to reject it entirely.

Our entire sample is biased toward things with Gaia DR2 data, but (in contrast to the other clusters in Papers I–VI), UCL/LCC is sufficiently close, and the stars are sufficiently not subject to reddening, that the bias toward the Gaia data is still likely to mean that the sample is representative of the true distribution, at least for sufficiently bright members (earlier than mid-M). Additionally, by discarding (or demoting) those stars that are apparently too far away, simply because they do not represent a large fraction of the sample, we are unlikely to introduce significant bias, even if those apparently distant sources really are 100–200 pc away. Kolmogorov–Smirnov (KS) and Anderson–Darling tests suggest that all the subsamples in Figure 5, truncated to <300 pc, are similar to each other; gold and silver are the most different, with silver having fractionally more of the slightly closer sources.

4. TESS Data

In this section, we obtain TESS LC versions from three different pipelines (Section 4.1). Source confusion and the contamination of LCs are major concerns with TESS LCs, and we discuss this in some detail in Section 4.2, along with some of the mitigation strategies for this that were developed in the context of looking for periods. The search for periods is presented in Section 4.3. In Section 4.4, we show that we are obtaining periods at least as reliably as others in the literature, especially for $P < 20$ days. We discuss the interpretation of these periodic signals (Section 4.5), and we finish with a summary of the limitations on the range of periods to which we are sensitive (Section 4.6).

4.1. TESS LC Versions

A primary driver for the inclusion of targets in this analysis is that there be a corresponding TESS LC from the first year of the mission. TESS covers most of the sky, but not all of it. We used TESS-Point (Burke et al. 2020) to assess which of our initial sets of stars could possibly have an observed LC in TESS’s first year of operations.

We created *eleanor* (Feinstein et al. 2019) 30-minute-cadence LCs for most of the candidate members of UCL/LCC, from TESS LCs from sectors 9–12. This approach provides three versions: PCA, principal component analysis; COR, corrected; and RAW. Some LCs were not successfully extracted, and thus some targets do not have *eleanor* versions. Additional 30-minute-cadence LCs from both the Cluster Difference Imaging Photometric Survey (CDIPS; Bouma et al. 2019)¹² and the MIT Quick-Look Pipeline (QLP; Huang et al. 2020a, 2020b)¹³ were available via the Mikulski Archive for Space Telescopes. Table 1 includes the numbers and sample fractions of those targets with LCs from each of the three data reductions.

In Figure 1, the obvious stripes of missing sources are primarily an artifact of TESS’s observation strategy. There is also an effective cutoff at both the bright and faint ends, where TESS saturates or there is an insufficient signal-to-noise ratio (S/N). The stars that are missing do not have LCs, either because they were not observed in the first year of the mission (“not on silicon”) or largely because they are too faint. The fact that we are missing some fainter stars is unsurprising. Figure 2 includes the K_s brightnesses for the targets analyzed here, with separate histograms for the sources with *eleanor*, CDIPS, and QLP LCs.

There is no reason to think that the unobserved wedges of the sky would introduce an astrophysical bias. TESS has unavoidable bright and faint cutoffs. In practice, the completeness for UCL/LCC falls dramatically for spectral types earlier than late F (no spots to cause periodic modulation) and later than roughly M5 (too faint to have an LC). However, there may be a subtle bias resulting from the fact that we do not have all the TESS LC versions for every source. Specifically, the *eleanor* LCs have many more outliers that could mask periods in the LCs, and, for many sources, they are our only choice. In an attempt to counteract the specific issues introduced by photometric outliers, we have spent considerable time on each source, to make sure that the best possible LC that we use does not have any obvious outliers, and we subsequently identify periods based on cleaned LCs. We are also missing LCs for a few faint sources, even when the targets are observable (see Figure 2), which biases our sample of periods against spectral types later than $\sim M4$ – $M5$.

4.2. Confusion and Contamination

Because the TESS pixels are $20'' \times 20''$, source contamination is a concern, especially given that UCL/LCC are in the Galactic plane and located toward the Galactic center. In Papers I–VI, based on K2 data, assessment of cluster membership was the dominant issue in assembling our final best set of targets and LCs to be analyzed. In the case of UCL/LCC, membership concerns play a more minor role, while source contamination becomes a much more significant concern when assembling the final best sample for analysis.

Because each LC was inspected by hand in order to look for periods (Section 4.3), in R.A. order, there were LCs that, we noticed immediately, were identical to another nearby (in projection) source’s LC in the set of candidate members. In the past, with the K2 LCs (Papers I–VI), we have been reasonably successful at teasing apart, through careful data reduction, the periods corresponding to each of any potentially confused targets, though we were unable to do so in a few cases. However, because the TESS pixels are so large, we have had to abandon, in most cases here, the hope of attaching individual periods to confused targets with much confidence. Thus, any stars where the LCs were identical to another nearby UCL/LCC star were discarded, without further analysis or discussion, except for rare occurrences where the stars were of much different brightnesses. In those cases, the period was attached to the brighter star, and the fainter star was discarded.

The total numbers of stars so affected are given in Table 1, and they make up the majority of the discarded (rejected) sources.

Stassun et al. (2018, 2019) assembled, as part of the TIC, a metric that attempts to quantify the degree to which a TESS LC is likely to be contaminated by nearby stars, and reported it as a

¹² <https://doi.org/10.17909/t9-ayd0-k727>

¹³ <https://doi.org/10.17909/t9-r086-e880>

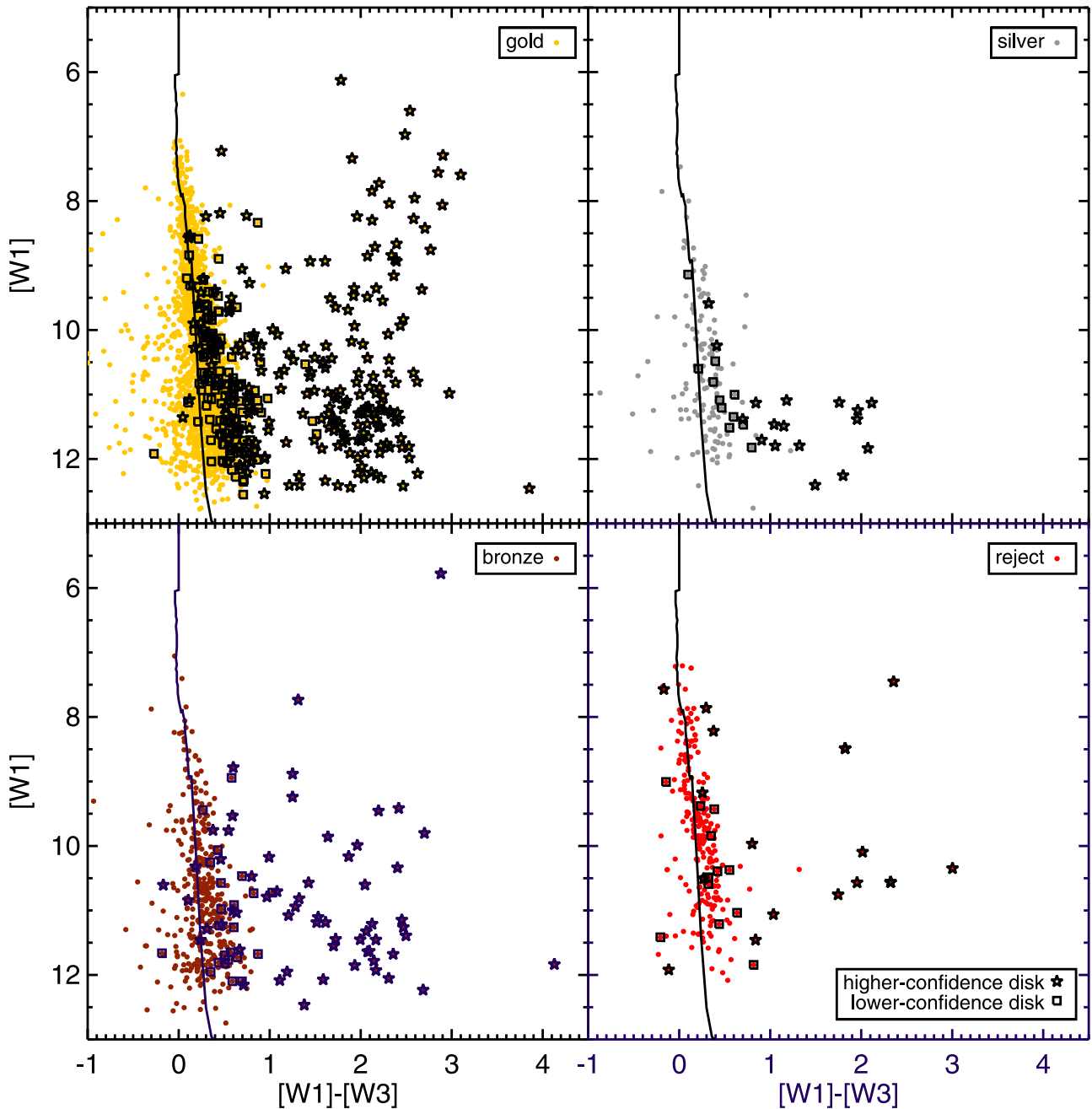


Figure 4. $[W1]$ vs. $[W1]-[W3]$ for the gold, silver, bronze, and rejected targets (see Section 2.3). High-confidence disks have an additional star and lower-confidence disks have an additional square. The black line marks the expected disk-free colors from Pecaut & Mamajek (2013). The points that are not identified as disks, but still appear in this plot to have significant $[W1]-[W3]$, are stars for which the only indication of an excess is a marginal $[W3]$ detection with a larger than typical error bar—that is, they do not have a significant excess. Conversely, stars with $[W1]-[W3]$ near 0 that are selected as disks are those that have an IR excess at wavelengths $>12 \mu\text{m}$. Most of the stars with disks are in the gold sample. Disked stars are not preferentially dropped from the member sample.

contamination ratio. This was assembled prelaunch, and makes a number of assumptions, so we did not rely solely on this value, but it was included in our assessment of whether to believe the TESS LC. Figure 6 shows the distribution of this contamination ratio for our targets as a function of brightness. Based on this and other similar plots, we decided that a TIC contamination ratio of 1.6 was an appropriate cutoff; targets with a contamination ratio >1.6 have a mark against them. As for our treatment of distances, the contamination flag could be unreliable, and so we downgrade (add a mark against) but do not a priori discard sources having a high TIC contamination ratio.

Stauffer et al. (2021), in looking for UCL/LCC members that were uncontaminated scallop shell stars, used a quick assessment of contamination. They compared the mean PCA flux in the LC to the Gaia DR2 G mag. Figure 7 does this for the ensemble, in order to identify those LCs whose mean flux seems inconsistent with the target’s measured G mag, suggesting that the LC is contaminated by flux from nearby stars. The black line in the left panel is given by $\log(\text{mean PCA flux}) = -0358 \times G + 8.45$. The targets above the black line in Figure 7 are ones that are tagged as having LCs that are likely contaminated, and those targets accumulate another mark against them. This calculation can also be subject to error, so

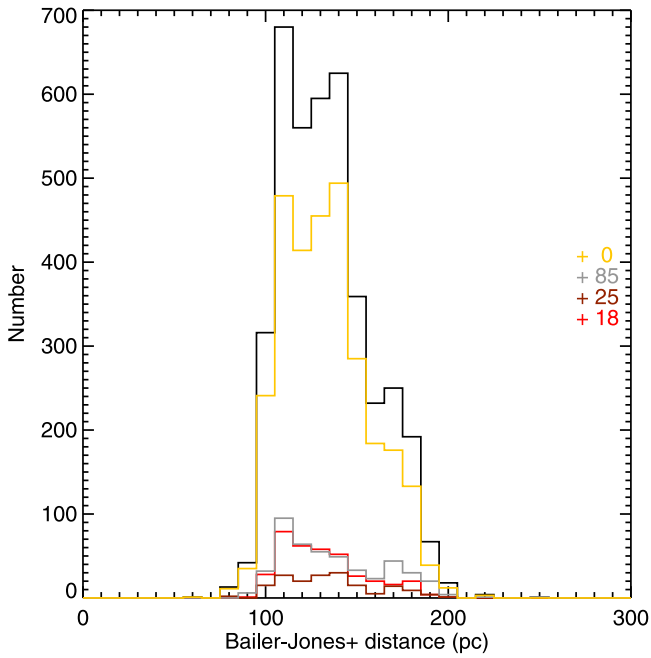


Figure 5. Histogram of the distances from Bailer-Jones et al. (2018) for the entire sample (black); the discarded targets (red); and the bronze, silver, and gold members (see Section 2.3). There are additional targets with a Bailer-Jones+ distance >300 , and those are indicated by the correspondingly colored numbers on the far right-hand side. Most of the sample (and all of the gold sample) straddles the range of the expected distances for UCL/LCC, ~ 100 – 200 pc.

this criterion is not enough, on its own, to discard the source. However, a lot of sources that have a high TIC contamination ratio also have an anomalously high PCA flux mean. Most of the sources in the bronze member bin have both a high TIC contamination ratio and a high TESS flux compared to the G magnitude (see Table 1).

Because not all of our targets have *eleanor* LCs, we do not have a mean PCA flux for all targets. Figure 7 also includes a similar analysis for the CDIPS LCs. This distribution is far better behaved than it is for the PCA LCs; the black line in this plot has the same slope as in the PCA plot. There are several reasons why the scatter is worse in the PCA version of this plot than in the CDIPS version. Because the LCs that emerge from the CDIPS analysis have far fewer outliers than the *eleanor* LCs, the mean CDIPS flux is a more accurate representation of the flux from the star. The CDIPS analysis was only performed on a subset of stars that are (a) cluster members, (b) show signs of youth, and (c) have $G < 16$ (Bouma et al. 2019). The *eleanor* LCs were calculated from lists of R.A./decl. and were therefore likely extracted even for stars that could be too faint/contaminated to expect a reasonable LC. The stars that are above the black line in the right panel of Figure 7 are tagged as possibly contaminated, even if they were below the line in the left panel. We note, for completeness, that the QLP LCs arrive normalized, so the approach adopted for the other LC sets will not work. Therefore, stars that only have a QLP LC cannot be identified as possibly contaminated using this approach.

In summary, the issues arising from TESS’s large pixels are significant. We lose several sources because we cannot identify with certainty which star is the origin of the variation seen in the extracted LC, and/or because effectively the same LC is returned for more than one target on our list. However, there is

no reason to think that a significant astrophysical bias would be introduced, based on the projected distance to a neighbor star bright enough to affect the LC. Later, more sophisticated LC extraction approaches might recover the LCs for some targets. We demoted stars to silver (one mark against), bronze (two marks against), or rejected them (three or more marks against), based on how likely we thought it was that the star was too far away (Section 3.5) or the LC was contaminated. Despite our best efforts to omit stars where source confusion was significant, it is likely that a few sources subject to source confusion still remain in our data, even in the gold subsample. We anticipate, however, that they are a small minority of the sources used here, particularly in the gold subsample.

4.3. Finding Periods in TESS Data

As in our earlier papers, we selected the “best available” LC version, this time from the products provided by *eleanor*, CDIPS, and QLP, when available. To identify significant periods, we used the Lomb–Scargle (Scargle 1982) approach, as implemented by the NASA Exoplanet Archive Periodogram Service¹⁴ (Akeson et al. 2013). We also used the IRSA Time Series Tool,^{15,16} which employs the same underlying code as the Exoplanet Archive service, but allows for interactive period selection. The period range searched was 0.05 days (1.2 hours) through 20 days. Stars with only one TESS sector have about a 30 day campaign (~ 24.1 – 26.9 days for these sectors), suggesting that the maximum plausible period should be about 15 days. About 12% of the targets have more than one TESS sector, so $P > 15$ days could be retrievable in those cases. In practice, no periods > 17.1 days were retained as plausible or reasonable.

Each LC was separately inspected by hand. Although an automatic 5σ clipping was imposed, many LCs had significant numbers of extreme outliers. More aggressive automatic clipping failed to remove all the outliers as well as inappropriately rejected points in LCs that did not have so many outliers. Such problematic outliers were manually removed and the Lomb–Scargle analysis was redone, as necessary. The period analysis was also performed with a maximum P of 2 days, in an attempt to limit the influence of additional occasional ~ 6 – 7 day timescales in the data that we assume are either instrumental or introduced in data reduction. The stars that appeared to have a period near that regime were subject to particular scrutiny, to ensure that they were plausible periods.

We retained up to four viable periods for each target. For the K2 clusters analyzed in Papers I–VI, about 20% of the stars are multiperiodic, but only $\sim 12\%$ of the members here are multiperiodic. There is no astrophysical reason to assume that the stars in UCL/LCC would be intrinsically less likely to be multiperiodic than the stars in Papers I–VI (which include both older and younger stars). We thus assume that the TESS LCs are more difficult to analyze using our approach, perhaps due to increased noise and/or shorter individual campaigns. However, this could be a selection effect. In the K2 analyses, M stars with multiple periods often turned out to be binaries. The Gaia analyses feeding into our membership lists may have, through the selections made in those papers, biased the samples against

¹⁴ <https://doi.org/10.26131/IRSA538>

¹⁵ <https://exoplanetarchive.ipac.caltech.edu/cgi-bin/Pgram/nph-pgram>

¹⁶ <http://irsa.ipac.caltech.edu/irsaviewer/timeseries>

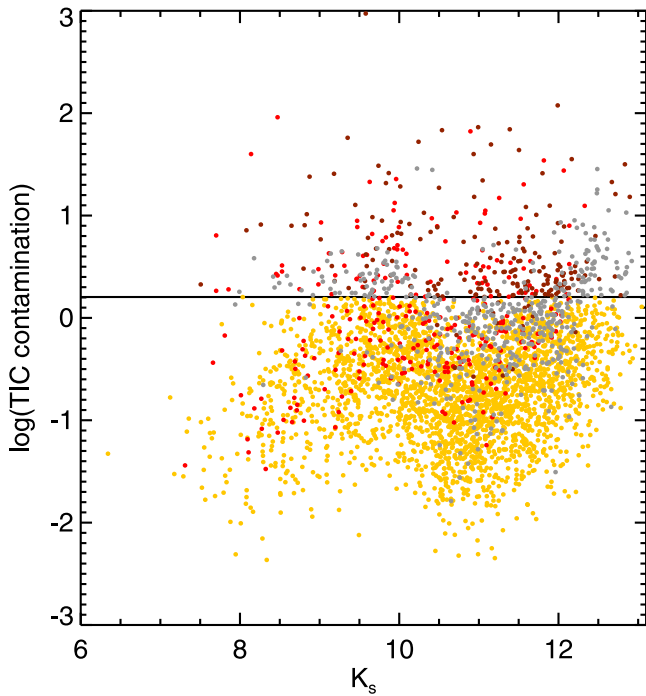


Figure 6. The log of the contamination ratio from the TIC (Stassun et al. 2018, 2019) plotted against K_s . The discarded targets are red; gold, silver, and bronze members are colored correspondingly. The horizontal line is at a contamination ratio of 1.6, a number that we arrived at by inspection (of this and other similar plots) as a reasonable cutoff between the LC being “likely contaminated” and “likely not or at least less likely to be contaminated.” Gold members (by definition) have a contamination ratio < 1.6 .

binaries (and higher-order multiples), so it may be the case that our initial member list is fundamentally less likely to include binaries. Therefore, if most multiple periods are due to stellar multiplicity, our source list is therefore less likely to exhibit multiple periods.

The periods that we derive appear in Table 2 for all members and in Appendix A for the discarded (rejected) targets. Note that we have included periods for all the periodic LCs, but for the discarded targets, the periods may very well not correspond to the stars as listed.

For about 10% of the entire sample, there were periods that could be ambiguous; for example, there seemed to be a strong peak in the power spectrum, but the phased LC was not as convincing as the remaining $\sim 90\%$ of the sample. These are indicated in the corresponding data tables (Tables 2 and 3). They are all fainter targets; see the last panel in Figure 2 for a histogram comparing the brightness of the high-confidence periods to that of the lower-confidence periods. None of these less confident periods are found in the gold sample—we note that no star was removed from the gold sample on the basis of having a questionable period.

4.4. Comparison to Literature Periods

As a check on our ability to match stars with the correct LCs, as well as retrieve accurate rotation periods, we compare our periods with those in the literature. Four studies monitoring targets in the optical have significant overlap with our targets, and several individual targets appear in a scattering of other papers. Figure 8 presents a comparison of the measured rotation periods, where all stars in common are included,

regardless of whether the source was ultimately dropped in our analysis. (Appendix B includes a list of the measured periods for individual comparison, plus notes.)

Kiraga (2012) reported periods from the All Sky Automatic Survey (ASAS). Because the positions as originally reported are not very precise, we took the counterparts as identified in Kiraga (2012), rather than matching anew by position. We have 162 stars in common. Mellon et al. (2017) have 70 stars in common with us; there are a few (see Appendix B) for which they discarded the P they obtained, but we independently recovered it, suggesting that the period is real. Gaia DR2 (Gaia Collaboration et al. 2018a) included rotation periods, and we have 43 stars in common. The All-Sky Automated Survey for Supernovae (ASAS-SN) catalog of variable stars (Jayasinghe et al. 2018) reports periods for 456 stars in common with us. Other rotation period data in the literature can also provide a comparison (Batalha et al. 1998; Wichmann et al. 1998; Strassmeier et al. 2005; Broeg et al. 2007; Christiansen et al. 2008; Messina et al. 2010, 2011; Alfonso-Garzón et al. 2012; Donati et al. 2012; Fruth et al. 2013; Kóspál et al. 2014; Desidera et al. 2015; Distefano et al. 2016; Siwak et al. 2016; Drake et al. 2017; Samus’ et al. 2017; Nicholson et al. 2018; Ripepi et al. 2019; Zúñiga-Fernández et al. 2021). There are a total of 56 such literature stars in common with us. The union of all the unique stars in our ensemble that have any period in the literature is nearly 600, about 15% of the ensemble.

The results on the whole are a mix of excellent agreement (the majority), likely harmonics reported in the literature, and, for a few, significant disagreement with the periods derived from the high-quality (but often subject to source confusion) TESS data. We recover most periods to better than 20%; see the percentages in Figure 8. Limiting the comparison to $P < 20$ days (where we have the highest likelihood of recovering periods with the TESS data), we recover a higher fraction of periods. In a few cases, the TESS LC has significant variations in the LC, such that even a period comparison $> 20\%$ could reasonably be considered a match. In some other cases, the literature reports a period similar to one that we had discarded as likely instrumental or less secure (see Appendix B); we did not go back and resurrect our retrieved period, since we do not have the ability to do so for all stars.

For each mismatched period < 20 days, we investigated the prior period(s) in comparison to the TESS LS, and we believe that the period(s) we report is/are the correct periods for these stars—or at least the LCs that we have associated with them—during the TESS campaign(s). Given the relatively coarse sampling rate of ASAS-SN compared to TESS, it is perhaps not surprising that many of the short periods reported by ASAS-SN are longer aliases of the periods that we find. It is encouraging that source confusion does not appear to be a factor in the overwhelming majority of cases.

4.5. Interpretation of Periods

Periodic behavior in stars can have different origins and interpretations, and the shape of the LC or the periodogram can shed light on the mechanism. Older clusters (Pleiades and Praesepe) have less diversity of LC shapes than younger clusters (USco, ρ Oph, Taurus, and Taurus Foreground); this is a result of circumstellar disks (both accretion from and occultation by disks). UCL/LCC is not as old as the Pleiades, but it is older than USco. Thus, we find LCs covering the full range of types identified in our earlier papers (Papers I–VI).

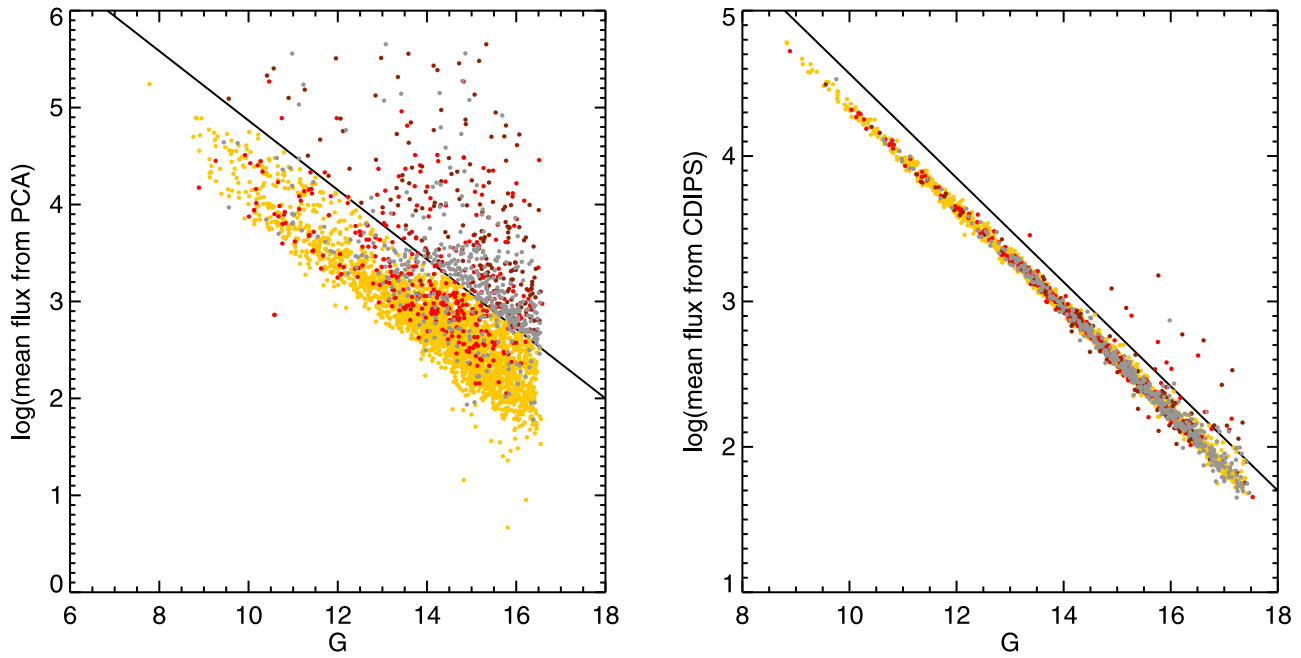


Figure 7. The log of the mean flux from the PCA *eleanor* LCs plotted against Gaia G (left), and the log of the mean flux from the CDIPS LCs plotted against Gaia G (right). The discarded targets are red; gold, silver, and bronze members are colored correspondingly. The black line on the left is given by $\log(\text{mean PCA flux}) = -0.358 \times G + 8.45$. The black line divides the stars whose G is much different than the mean PCA LC flux from those whose G seems appropriate given their mean PCA flux; stars above this line are likely to be contaminated by neighbors. Gold members (by definition) have a mean PCA flux consistent with their G . Not every one of our targets has an *eleanor* LC, so the right plot repeats the analysis using CDIPS; the black line is the same on the right, just shifted down by 0.3 dex. The scatter is worse for the *eleanor* LCs (left plot) than for the CDIPS LCs (right plot), because there are many more outliers in the *eleanor* LCs.

Here, we briefly summarize the physical interpretation of the observed LCs. Table 1 collects all the counts and sample fractions.

4.5.1. The Straightforward Rotators

About 90% of the members are periodic (see Table 1). Of those, >60% of the stars are sinusoidal periods, or close to sinusoidal periods. These are all consistent with variations due to a starspot on the surface rotating into and out of view. Some stars have >1 period, though we use the first period reported in most of this analysis. We find all the same types of rotational variables as in Papers I–VI (see Table 1). The categories are: single-period (one spot or group rotating into and out of view), multiperiod (more than one spot or group rotating into and out of view), binary (or higher-order multiple, each with a spot/spot group rotating into and out of view), double-dip (two spots/spot groups rotating into and out of view), moving double-dip (two spots/spot groups rotating into and out of view that are moving/evolving with respect to each other and/or latitudinal differential rotation), shape changers (spot/spot group evolution and/or latitudinal differential rotation), beaters (>1 close P ; multiple stars or latitudinal differential rotation), complex peak (spot/spot group evolution and/or latitudinal differential rotation), resolved close peaks (>1 close P ; multiple stars or latitudinal differential rotation, or source confusion), and resolved distant peaks (>1 very different P ; multiple stars or source confusion).

Separately, there are pulsators, typically manifesting as a forest of very short periods, but in the case of TESS these can also manifest as just a very short period. In our K2 work, we found in many cases that the strongest peak of those pulsators is likely closely related to rotation, based on where such stars fall in the P versus color diagrams. We also have five stars with

phased LCs that resemble those of RR Lyr stars, but at significantly faster periods; we have identified them as possible pulsators. In the present analysis, we have left the pulsation periods in the sample, but removed them from the plots. They are listed in Appendix C.

The sample fractions and numbers for these LC types in UCL/LCC are in Table 1, which could be compared to Table 3 in Paper VI, which includes the same analysis for all the clusters in Papers I–VI. Direct comparison is somewhat complicated, however. With more than 3500 member stars, the UCL/LCC member sample has more than three times as many stars as our USco member sample, more than four times as many as our Pleiades member sample, and more than 20 times as many as Taurus or ρ Oph. With the various issues affecting the periods that we can find using the TESS data (see Section 4.2), it may not be fair to compare, e.g., the fraction of multiperiod stars between TESS and K2, or the fraction of stars that are shape changers, when the noise characteristics of TESS are so different than K2. Overall, the fraction of periodic stars is in line with what we expect for a situation where some of the stars have circumstellar disks. Detailed comparison beyond that may not be easily possible until we have more experience with TESS data—more specifically, until we understand the noise characteristics well enough to know if we are incorrectly categorizing some of the TESS LCs using the classes developed with K2 data.

4.5.2. The More Complex Rotators

Stauffer et al. (2017) discussed stars that were then identified as scallop shells, flux dips, and transient flux dips. These unusual LCs have sharp angular features in the *phased LC*, which are too broad for planets and too small for spots. Most such sources are fast-rotating disk-free M stars. We interpreted these LCs as being due to matter entrained in coronal loops

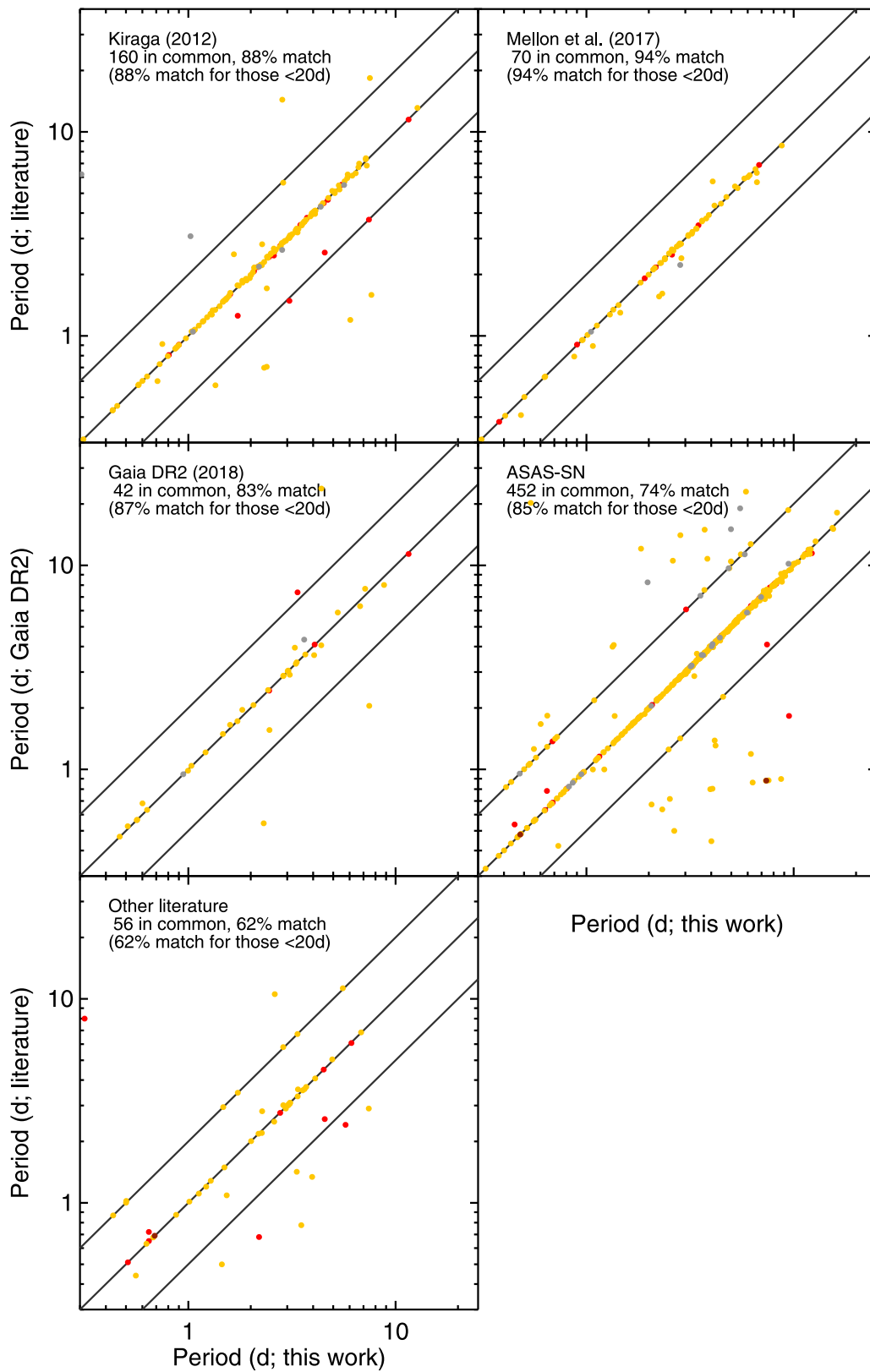


Figure 8. Comparisons of the periods derived here with those found in the literature. Upper left: Kiraga (2012) periods; upper right: Mellon et al. (2017) periods; center left: Gaia DR2 periods; center right: ASAS-SN periods; lower left: all other literature (see the text and Table 4). Periods >20 days are not shown. In all panels, the gold, silver, and bronze members are indicated, along with the discarded sources (red); note that some of the discarded sources are rejected because the period in the LC cannot be securely tied to an individual source. Most periods agree well; the percentages quoted in the figure indicate the periods matching within 20% overall and just for those periods reported in the literature to be <20 days. Note that most points in these plots fall on the 1:1 line.

(Stauffer et al. 2017). Stauffer et al. (2018a) found more, as did Zhan et al. (2019), Bouma et al. (2019), and Günther et al. (2022).

Stauffer et al. (2021) identified ~ 30 such objects in UCL/LCC, based on early explorations of the data we present here. After a more complete analysis, we find ~ 100 stars in total (~ 70 new) in this LC category (see Table 1 and Appendix C). Due largely to the lower S/N in the LCs, some of these new candidates may not be as unambiguously identifiable as the scallop shells/flux dips in Stauffer et al. (2021). While most of the scallop shells/flux dip LCs can be linked to specific stars, two of the stars from Stauffer et al. (2021) are unfortunately identified here as being clearly confused with other sources (TIC 89026133 and 89026136; see Section 4.2 and Appendix C). Several other targets with these kinds of LCs are also currently impossible to link to specific stars. Secure identification of exactly which star is creating the patterns awaits a later investigation.

The fact that we have ~ 100 stars in this LC category is not surprising. The previous literature has shown that these LCs occur more frequently in younger clusters. Fractionally, we have found them to be $\sim 1\%$ of the Pleiades sample, $\sim 3\%$ of the USco sample, and $\sim 4\%$ of the Taurus sample, so it is not at all surprising to find $\sim 3\%$ among our UCL/LCC sample; the fraction is consistent with the discovery rate in other young clusters studied with K2.

Stauffer et al. (2021) also identified a star described there as having “icicle-like” features in the LC, arising from a beating between the intrinsic period (where the shape of the LC involves a dip) and the TESS sampling rate. In that case, it was a photometric binary with two periods. Now, with the larger member sample, there are a few more LCs exhibiting this broad characteristic, some of which have only one period, and few of which are obviously binaries. We have simply identified them as being periodic at the appropriate period. Some of the “icicle” stars have dips suggestive of eclipsing binaries (EBs).

There are many obvious EB LCs among the UCL/LCC stars, and some additional LCs that could be EBs or could be flux dips. Of the EBs, in some cases, we can omit the eclipses and still derive a rotation period from the photospheric component of the LC. We have listed the P_{rot} in the tables (and used those in the plots). In Appendix C, we have listed the EBs (and candidates), along with the P_{binary} , where we can derive it.

We tabulate “timescales” for LCs with repeating patterns that are probably not rotation periods in Appendix D.

4.5.3. The Disk-influenced Periodic Patterns

Some stars in UCL/LCC still retain their disks, and they exhibit LC types associated with circumstellar material, namely dippers and bursters (see, e.g., Cody et al. 2014; Cody & Hillenbrand 2018; Cody et al. 2022). These sources have a “continuum” LC that is punctuated by dips (fading) or bursts (brightening). Dippers are interpreted as occultations by disk material, while bursters are interpreted as accretion impacts. These stars all have large IR excesses.

Note that the LCs identified as being bursters or dippers are identified as such without reference to the SED; they all turn out to be disked, however, based on the SED.

Tajiri et al. (2020) also identify dippers from TESS full-frame images. Among their sample, we independently identified

TIC 226241509, 243324939, 266079454, 334999132, and 412308868 as dippers in this work.

4.6. Range of Periods

In addition to the brightness and faintness limits imposed by the TESS data availability, we are limited by the TESS cadence in the range of P to which we are sensitive. The shortest reliable period that we have identified is 0.436 days (=1.05 hr); the longest is 17.1 days. Our range of identified periods is comparable to the range that we expect for stars with ages similar to the UCL/LCC clusters.

Our approach to finding periods in the TESS data has to include star-by-star inspection and refinement after initial automatic processing, despite the potential for biases introduced by this human-based process. It enables us to easily find targets that are subject to obvious source confusion (Section 4.2). There are enough very large outliers in the LCs, and a suspiciously common $\sim 6\text{--}7$ day period (which we suspect is instrumental or introduced by LC extraction), such that the investment of time per star is well spent. Given the comparison to the literature, we suspect that we may have conservatively dropped some legitimate $\sim 6\text{--}7$ day periods. While no one else in the literature to our knowledge has reported problems with $\sim 6\text{--}7$ day periods, others have reported difficulty with $P > 27$ days (see, e.g., Avallone et al. 2022, and references therein); we do not have any periods that long.

It can be harder to obtain rotation periods for disked stars as a result of stochastic contributions from the disk and/or accretion (see, e.g., Cody & Hillenbrand 2018, and references therein). Among all the disked stars, the periodic fraction is $\sim 85\%$, to be compared with $\sim 90\%$ of the nondisked stars (Table 1). Thus, our periodic member sample is likely biased against disked stars for astrophysical reasons.

5. UCL/LCC Color–Magnitude and Period–Color Diagrams

In this section, we present the UCL/LCC sample in the Gaia-based absolute color–magnitude diagram (Section 5.1), in the K_s versus $(V - K_s)_0$ observed color–magnitude diagram (Section 5.2), and in the period versus $(V - K_s)_0$ diagram (Section 5.3). In each case, we discuss how the subsamples are similar or different in these diagrams.

5.1. Gaia Color–Magnitude Diagrams

Figure 9 presents absolute Gaia color–magnitude diagrams for the three member samples (gold, silver, and bronze) and the rejected sample. The stars that appear to be significantly above the zero-age main sequence (ZAMS) or near ZAMS, as defined by the rest of the sample, are immediately apparent; these are candidate giants or other NMs. Our gold sample is defined as having none of these stars included. A significant fraction of the silver members (Table 1 and Figure 9) have as the one mark against them only a discrepant Bailer-Jones distance.

At first glance, the ZAMS looks similar in all of the member subsamples (gold, silver, bronze). Omitting all of the giants and using a two-dimensional two-sided KS test in addition to histograms of color or absolute G , we can compare the member subsamples in more detail. The gold sample has, by far, the most well-populated early ZAMS, down to about $G_{\text{BP}} - G_{\text{RP}} < \sim 2$ (and $M_G \sim 7$), such that it is still significantly different from the other subsamples, even after omitting the giants. This makes

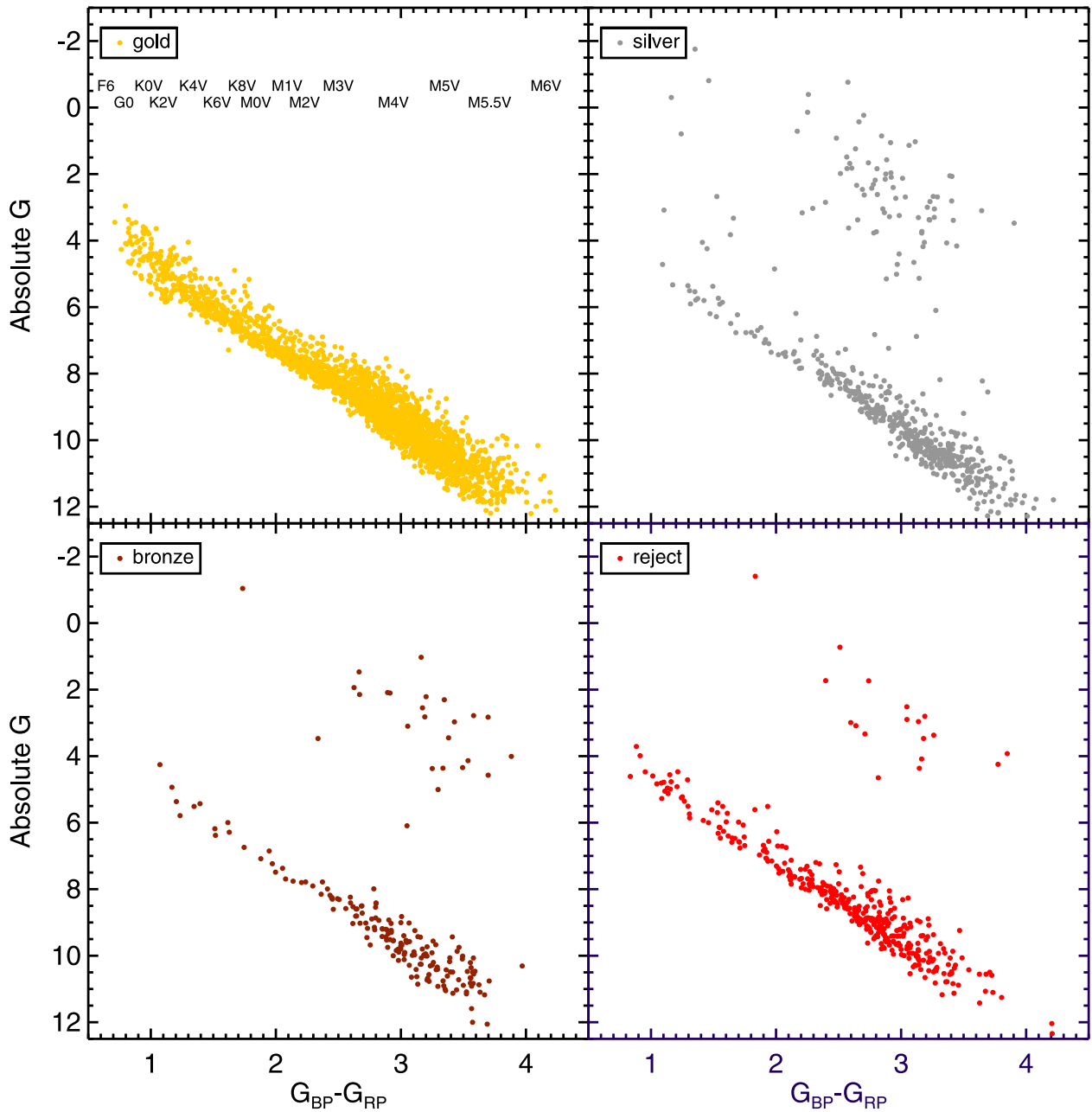


Figure 9. Absolute Gaia color–magnitude diagram, using distances from Bailer-Jones et al. (2018), for the gold, silver, and bronze members, and the rejected targets (see Section 2.3). The stars that appear to be giants (or are even just significantly above the ZAMS defined by the rest of the sample) are immediately apparent. The gold member sample, by definition, has no objects with Bailer-Jones distances >300 pc.

sense, as the brighter stars will be easier to measure and should therefore be easier to identify as secure members. The silver and bronze subsamples are most similar to each other, with fractionally more fainter stars than the other subsamples near $G_{BP} - G_{RP} < \sim 3.2$.

As in Figure 9, the JHK_s diagrams presented above in Figure 3 also suggest that all the member subsamples are similar. In detail, though, the gold sample has more early-type stars, making it different at a statistically significant level, while silver and bronze are the most similar.

5.2. V and K_s Color–Magnitude Diagrams

Figure 9 shows a tightly constrained empirical ZAMS, but Gaia data are not available for most of the stars in the other

clusters in Papers I–VI. Papers I–VI used $(V - K_s)_0$ as a proxy for mass, and to facilitate the comparisons that we wish to make here, we employ $(V - K_s)_0$ colors for UCL/LCC as well, over the readily available and reliable Gaia colors.

Figure 10 shows the observed (not absolute) K_{s0} versus $(V - K_s)_0$ diagrams for our UCL/LCC member sample, revealing a cluster locus that is broader than expected, given Figure 9. A significant contributor to the scatter in Figure 10 comes from the variations in distance across UCL/LCC members. The gold sample spans the entire range of $(V - K_s)$ colors, and the M stars are particularly well populated. The silver and bronze samples do not span the full range of $(V - K_s)$, and have fractionally fewer M stars. Nearly all the stars are periodic (Table 2). Figure 10 also reveals that there is more scatter in the rejected targets than the other subsamples,

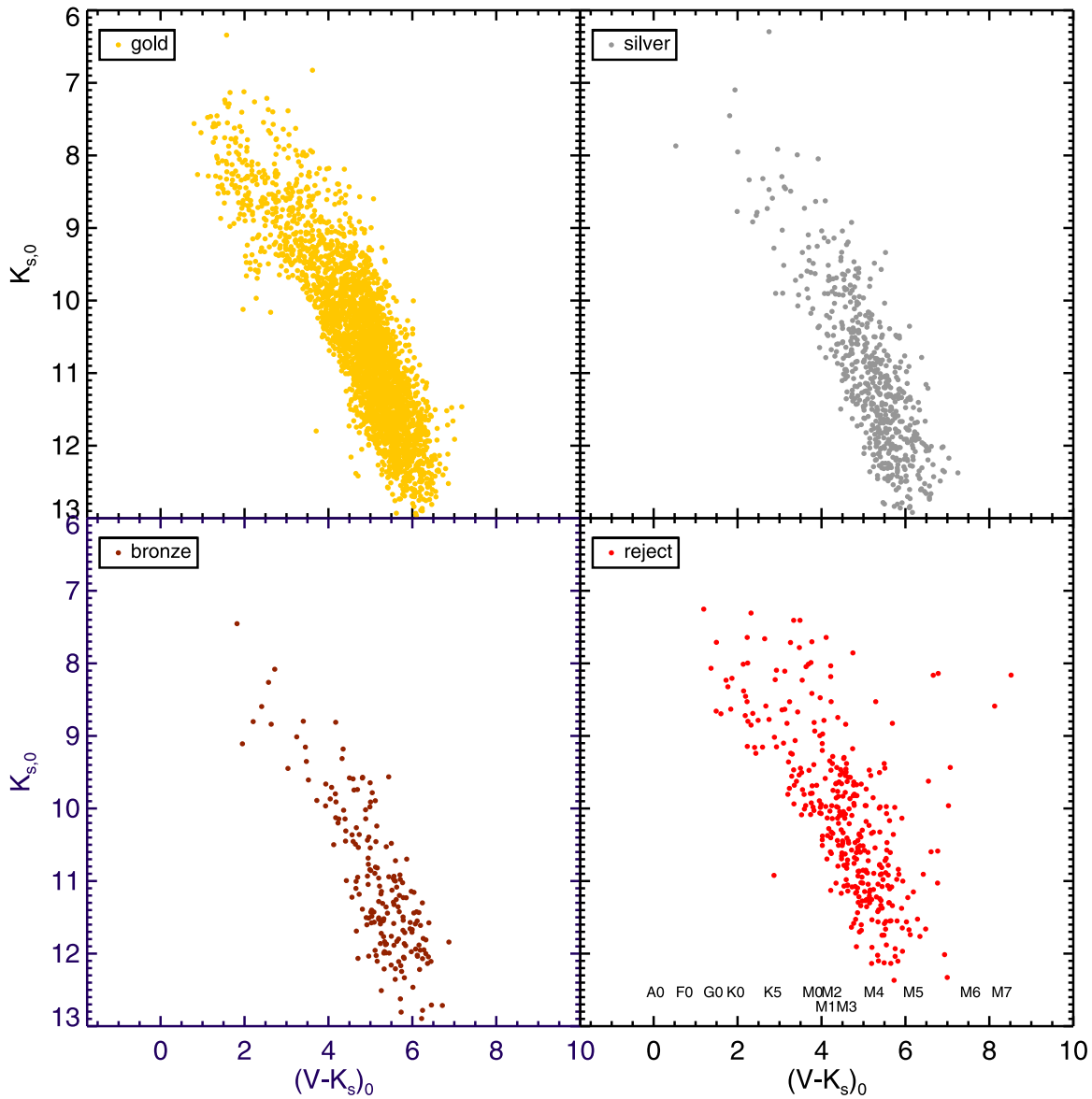


Figure 10. Dereddened K_s vs. $(V - K_s)_0$ for the gold, silver, and bronze members, and the rejected targets. The gold sample is the most well-populated across the full color range. There is more scatter here in all the member subsamples than in Figure 9, in part because the stellar distances vary significantly over the cluster. The discarded sample has the most scatter, which makes sense, given that source confusion is important for many of the rejected stars.

which makes sense, particularly if there is source confusion, even in 2MASS.

5.3. Period–Color Diagrams

Figure 11 shows the P versus $(V - K_s)_0$ plot for the members and rejected targets in UCL/LCC. Both the P and $(V - K_s)_0$ values are listed in Table 2 (or Table 3 for the rejected targets). As in our K2 rotation papers, for stars with more than one period, we have taken the first period and the identified $(V - K_s)_0$ as being representative of the same star (likely the primary, if it is a multiple).

The gold sample has clear structure in P versus $(V - K_s)_0$. Most of the M stars are organized into a sequence of steeply increasing rotation rate (decreasing periods), going from early M through at least M4/M5. The higher-mass stars (G and K spectral types) have considerable scatter, but they seem to be, on average, more slowly rotating than most of the M stars, with the Gs also rotating much faster than the Ks. The bronze and

silver distributions seem to have similar structure, but there are too few stars to define it clearly. It is unsurprising that the rejected stars have the most scatter, since it is less likely here that the measured P goes with the assumed $(V - K_s)_0$.

Anticipating discussion later in the paper, the scatter found in Figure 11 is substantial, even for the gold sample. In other clusters, any scatter had been a result of reddening corrections or unresolved binaries. Reddening corrections are not as big a concern in UCL/LCC (Section 3.3). There is not enough literature for us to constrain significantly the binary fraction among our UCL/LCC member sample, though any such binaries would have had to survive the culling based on accurate Gaia measurements, which is likely to omit binaries.

If we look at the fraction of stars that have more than one period, as a function of location in the P versus $(V - K_s)_0$ plot, the multiperiod fraction rises steeply on the edges of the structure traced by the bulk of the points. With TESS, especially given the apparent relative difficulty of finding

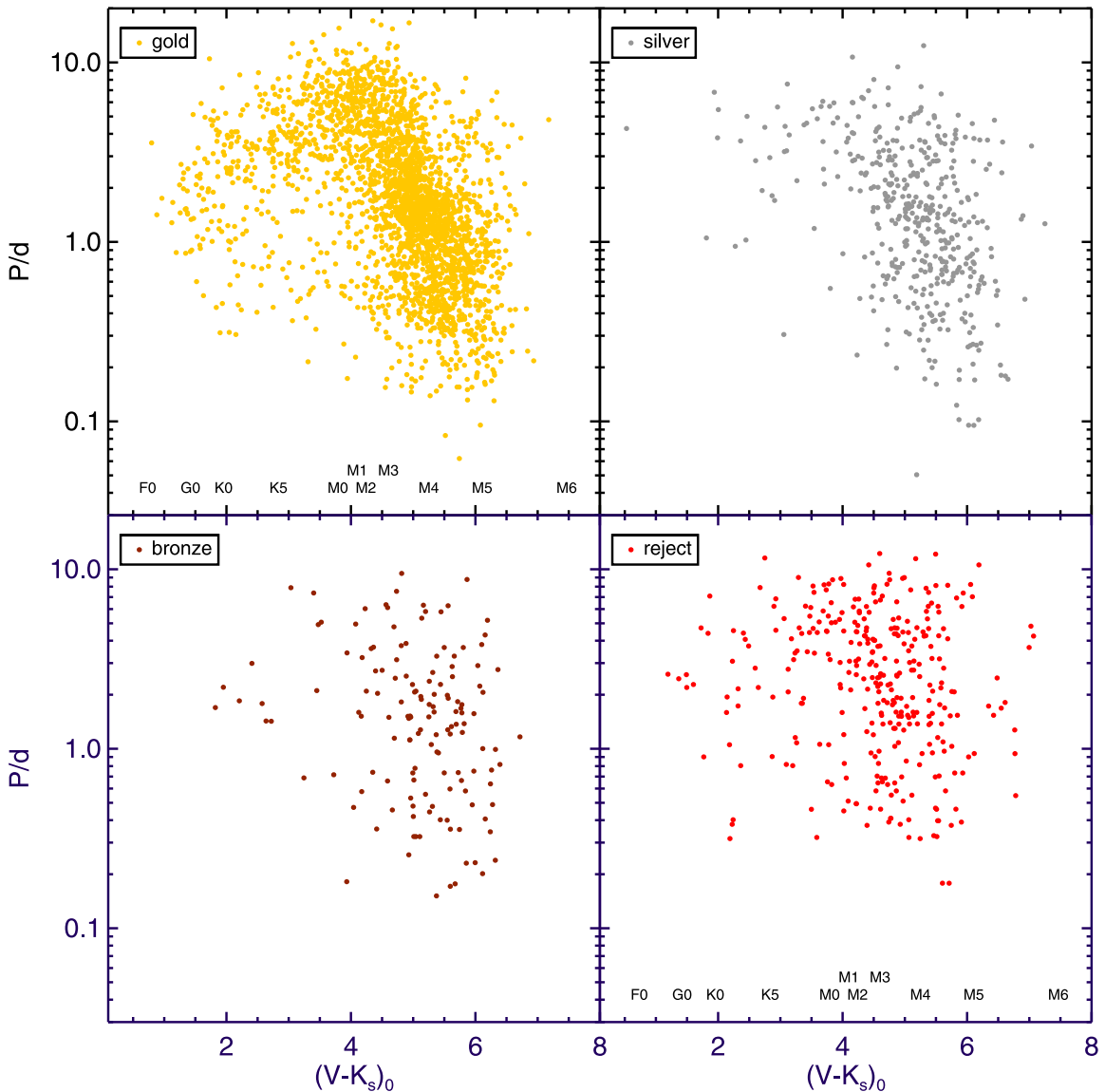


Figure 11. P (in days) vs. $(V - K_s)_0$ for the gold, silver, and bronze members, and the rejected targets. Note that there are two stars from the discarded sample with $(V - K_s)_0 > 8$, beyond the plot limits. The gold sample is the best populated and, in this distribution, it is easiest to see structure in. The structure is similar to that found in other clusters; see the text and Figure 12.

multiple periods (Section 4.3), without additional data, we cannot be sure that the outliers in P versus $(V - K_s)_0$ are photometric binaries, or are instead primarily a result of source confusion affecting the P attributed to a given star. Given the likely bias against binaries from Gaia, we have to suspect that source confusion is a factor.

As the UCL/LCC sample is large, and there is some evidence for the variation of stellar ages across the association, we explored whether or not there is any evidence for changes in the distribution of P versus color across the sky in various member subsamples. We did not find any evidence for this.

6. Period–Color Distribution in Context with Other Clusters

In this section, we put UCL/LCC in context with the other clusters that we have studied with K2 data. We assume that the stars in UCL/LCC represent snapshots in time of the same population as found in the other clusters (e.g., Coker et al. 2016). We note as well that the rotation evolution is likely

influenced by the local UV environment (see Roquette et al. 2021), which would matter locally if the high-mass stars in UCL/LCC have influenced the local star evolution. We first compare the entire distribution of UCL/LCC to well-populated clusters (Section 6.1), then narrow this down to consider just the disk-free M stars in those clusters (Section 6.2). Next, we put UCL/LCC in context with the rotation rates from eight other clusters studied with K2 (Section 6.3), some of which are very sparsely populated. Finally, we consider the influence of disks, particularly among the M stars (Section 6.4).

6.1. Comparing to Well-populated Clusters

The period–color structure in UCL/LCC that is most obvious in the gold sample is suggestive of something intermediate between the distribution in USco (Paper V) at ~ 8 Myr and the Pleiades (Paper I) at ~ 125 Myr, which is consistent with the accepted age of UCL/LCC of ~ 16 Myr. Figure 12 shows UCL/LCC (just the gold member sample) in context with the most well-populated clusters that we have

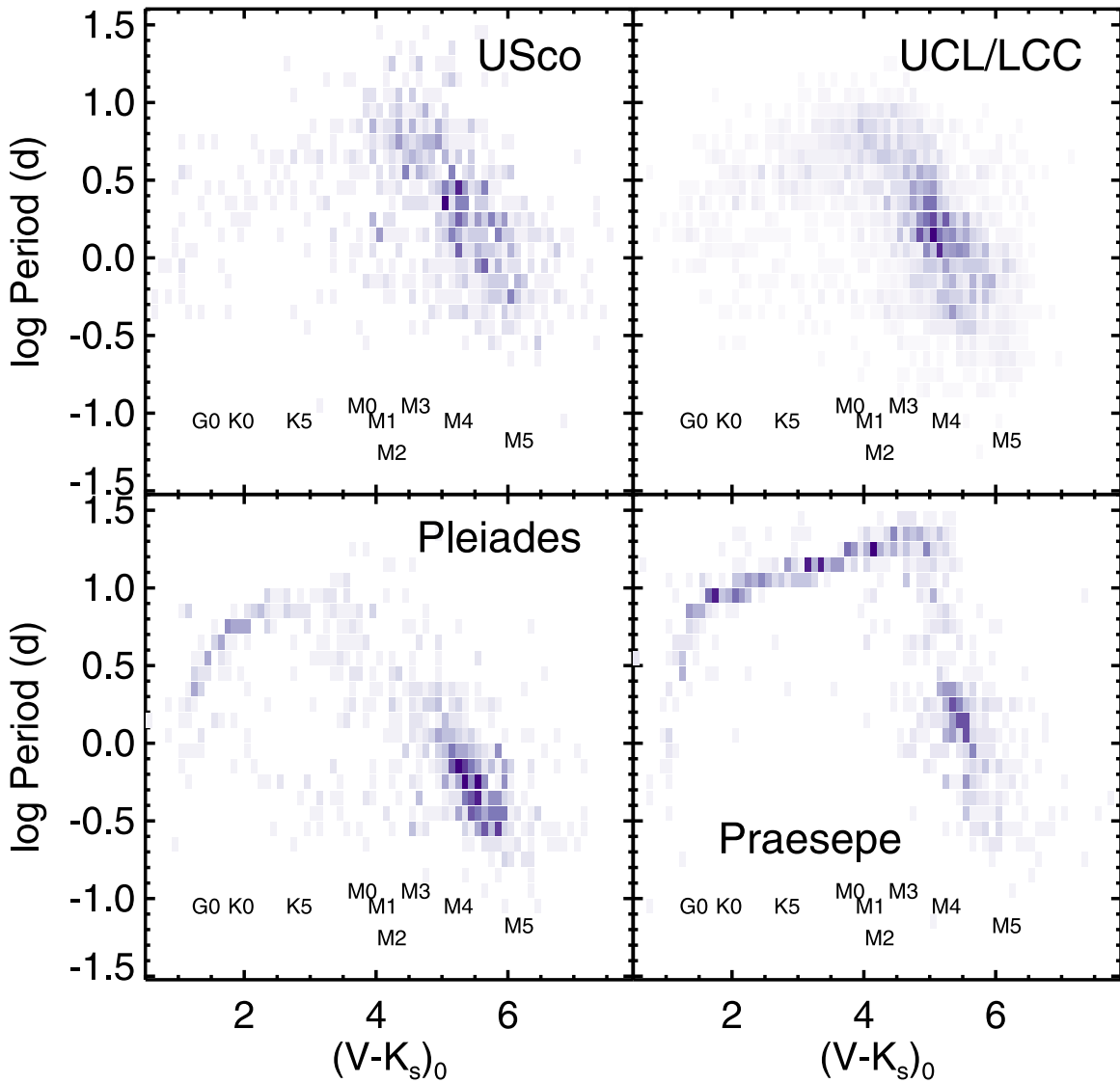


Figure 12. P (in days) vs. $(V - K_s)_0$, with disks removed: density maps, where the darker shades indicate more sources in those cells. Each cluster is self-normalized, such that the darkest shade is the best populated within that cluster, which is a different absolute number (and sample fraction) in each cluster. At the high-mass end, the distribution is well defined in Pleiades and Praesepe, but much less so in USco or UCL/LCC (which is just the gold member sample). The low-mass end is well defined in all four clusters. See the text for more discussion.

studied using K2: USco, Pleiades, and Praesepe (Paper IV; 790 Myr). In this plot, all the disks (secure and possible) have been removed from USco and UCL/LCC, leaving just the disk-free stars. The density map shows where the sources are clustered more tightly; there are so many stars, especially in UCL/LCC, that it is hard to appreciate the point density if only individual points are plotted.

The distributions of the G and K spectral types, which are very obvious and well defined by the Pleiades age, are far less obvious in the younger UCL/LCC, and even less obvious in the yet younger USco cluster. In Paper V, we suspected that the reddening in USco, which is patchy and sometimes large, meant that uncertainties in the reddening correction added artificial “smearing” to the distribution, rendering the higher masses so that they appeared to be less organized. However, in UCL/LCC, there is far less reddening, and less patchy reddening (Section 3.3 and Figure 3), yet the early-type “branch” is still not anywhere near as organized as in the Pleiades. The most extreme outliers in UCL/LCC may be

subject to source confusion (Section 5.3), but much of this “disorganization” may be a real feature of this rotation distribution for G and K spectral types in clusters $\lesssim 20$ Myr old.

6.2. Comparing the M Stars in the Well-populated Clusters

Most of the stars in the present analysis are M stars, and Figure 13 highlights their behavior across the clusters. Again, disks have been removed from USco and UCL/LCC, so these are just the disk-free gold member M stars. The top row has a linear fit to the M stars, and the bottom row includes running medians and scaled running medians. Paper V pointed out that the M-star slope between USco and Pleiades is the same, just shifted as the stars contract onto the main sequence. UCL/LCC fits neatly in between USco and Pleiades, with a slope that is indistinguishably the same. The slope for USco/UCL-LCC/Pleiades is vastly different than the slope for Praesepe, which makes sense, since the M stars are spinning up through the Pleiades, and spinning down by the older age of Praesepe, likely incorporating wind braking (Paper V).

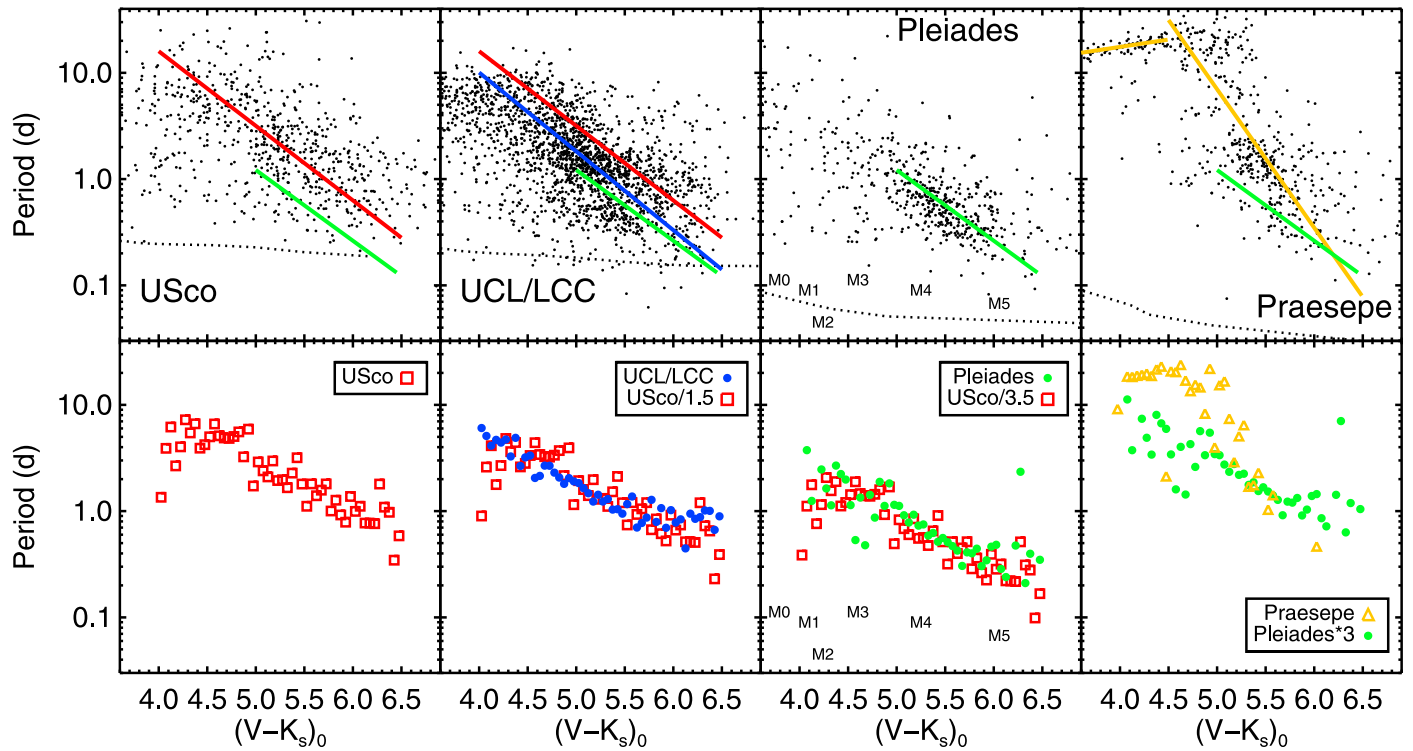


Figure 13. P (in days) vs. $(V - K_s)_0$ for M stars, with disks (high-confidence and possible) removed, and just UCL/LCC gold members. Top row: observations (the dotted lines are breakups); bottom row: medians of the observations in $(V - K_s)_0$ bins. Column 1: USco; Column 2: UCL/LCC; Column 3: Pleiades; and Column 4: Praesepe. In the top row, USco fit: red line; UCL/LCC fit: blue line; Pleiades fit: green line; and Praesepe fit: yellow line. In the bottom row, USco binned data: red symbols; UCL/LCC binned data: blue symbols; Pleiades binned data: green symbols; and Praesepe binned data: yellow symbols. The USco binned data are shifted in the second panel to match UCL/LCC, and shifted in the third panel to match Pleiades. Pleiades is shifted in the fourth panel to attempt to match Praesepe. UCL/LCC fits neatly in between USco and Pleiades, with a slope that is indistinguishably the same.

In both Figures 12 and 13, particularly for UCL/LCC, it is apparent that there is a denser region of points near $(V - K_s)_0 \sim 5$ mag, $\log P \sim 0.15$ ($P \sim 1.4$ days). This dense peak is very obvious in UCL/LCC, and far less prominent in the other clusters. In USco, the distribution is more diffuse, and the peak occurs at the same $(V - K_s)_0$, but slightly slower $\log P \sim 0.35$ ($P \sim 2.2$ days). For the Pleiades, the distribution is elongated along the entire distribution of M stars, but the peak is much redder and faster, at $(V - K_s) \sim 5.55$, $\log P \sim -0.25$ ($P \sim 0.56$ days). The Praesepe M stars have an entirely different distribution. The M-star peak is actually on the slow branch, at $(V - K_s) \sim 4.15$, $\log P \sim 1.25$ ($P \sim 17$ days); removing the slow branch, the peak is at the same color as the Pleiades, $(V - K_s) \sim 5.55$, and about the same period as UCL/LCC, $\log P \sim 0.15$ ($P \sim 1.4$ days).

There are several stars with very fast periods, apparently faster than breakup in some cases; they are found in all of the member subclasses, and some appear to have IR excesses. Those LCs, and their periods, appear legitimate and unambiguous, leading us to conclude that perhaps something may be wrong with the linkage between the LC and the stellar source. In cases where the apparent IR excess originates in a single band at WISE-3 or WISE-4, the possibility exists that the relatively low spatial resolution of WISE is also subject to source confusion, so neither the P nor the IR excess may be correctly tied to the star associated with the $(V - K_s)_0$; further exploration of these cases, with higher-spatial resolution data, is needed.

6.3. Comparing to Other Clusters

Figure 14 shows the data from UCL/LCC in context with all the other space-based rotation rates from K2 from our prior

work. For each cluster, an older well-populated cluster is underplotted to guide the eye regarding the evolutionary patterns. The UCL/LCC distribution is in the middle of the evolutionary age sequence. The structure in the Hyades is indistinguishable from that in Praesepe. In the case of the Taurus Foreground, there are so few stars that it is hard to identify any structure unique to that cluster. At the youngest ages, determining the structure is greatly complicated by the uncertainties added by the “smearing” imposed by reddening corrections and contributions from disk excesses. The structure seen in USco is vaguely apparent in Rho Oph, Lagoon, and Taurus. In the case of Lagoon, limited sensitivity complicates interpretation at lower masses.

In all of the three youngest clusters, there are relatively few stars, there is additional smearing due to reddening corrections, and there is a substantial disk fraction. The disks appear to affect the rotation distribution. Most notably, there is an obvious ~ 2 day pileup of disks in USco, as well as in UCL/LCC. We investigate the influence of disks in the next subsection.

6.4. Disks and Rotation

Figure 15 shows where the disks are on the sky, using the same orientation and units as Figure 1, but with a different interpretation of the point color. The disks in USco are as in Paper VI; high-confidence and lower-confidence disks in UCL/LCC are identified here and comprise $\sim 7\%$ – 8% of the sample. There are obvious clumps of stars with disks, but little large-scale systematic structure. There is also no obvious systematic difference (in distribution or disk fraction) between

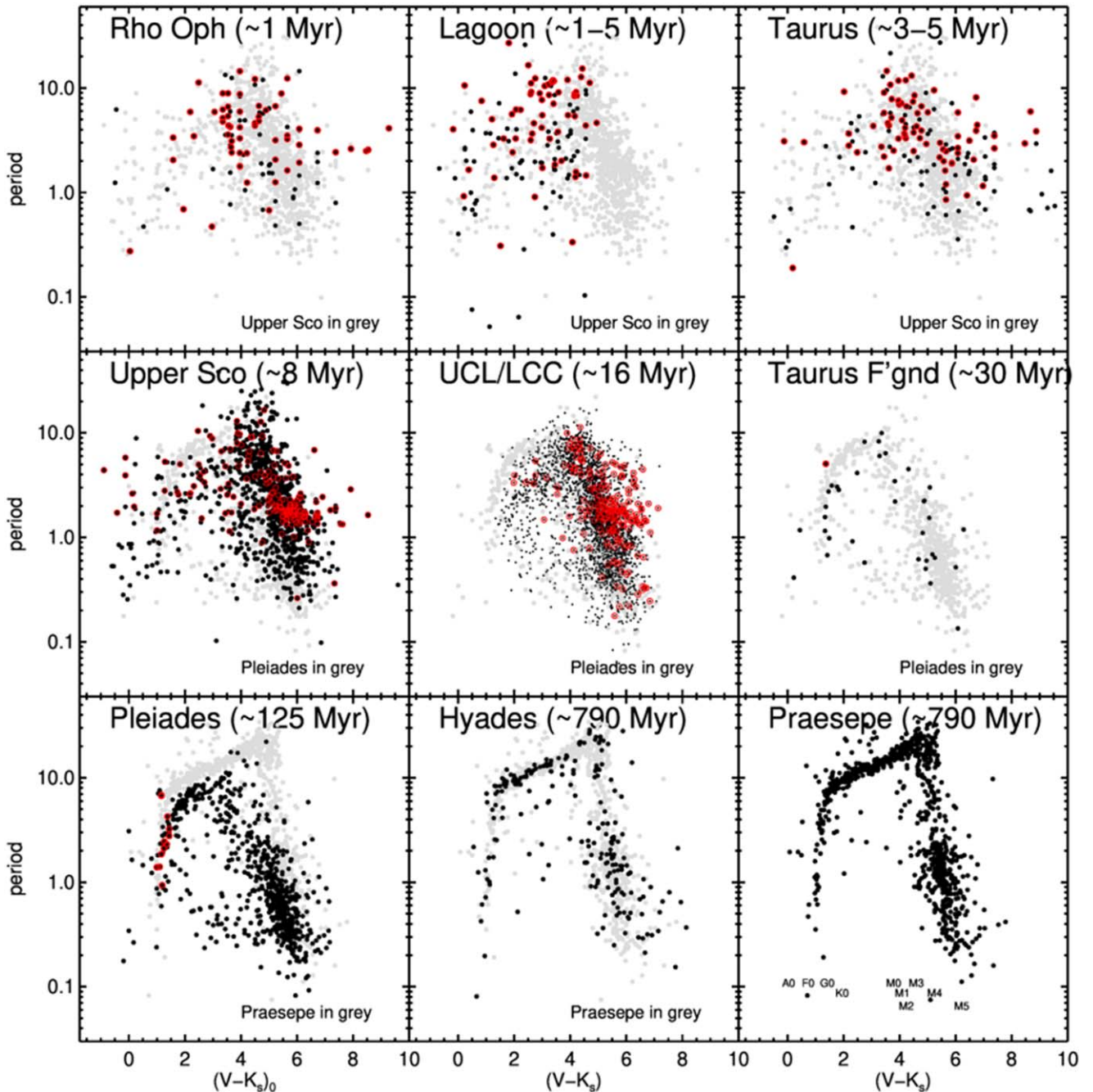


Figure 14. P (in days) vs. $(V - K_s)_0$ for all stars in nine clusters, all from K2, except UCL/LCC. Stars with IR excesses (e.g., disks) are shown with an additional red circle. The first row has the youngest, most populous cluster, USco, underplotted in grey. The second row has the Pleiades underplotted in grey. The third row has Praesepe underplotted in grey. The points are smaller for UCL/LCC because there are so many points that it is hard to see the patterns otherwise. The UCL/LCC points are all from the gold member sample. It again seems to fit well “in sequence” with the other clusters around it. References for data—Rho Oph: Paper V; Lagoon: Rebull et al. (in preparation); Taurus: Paper VI; USco: Paper V; UCL/LCC: this work; Taurus Foreground: Paper VI; Pleiades: Papers I and II; Hyades: L. M. Rebull et al. (2022, in preparation); and Praesepe: Paper IV.

UCL and LCC; given their similarity in age, this is not surprising.

There is a theoretical expectation that primordial disks lock the rotation rate of the star to that of the inner disk (e.g., Ghosh et al. 1977; Königl 1991). When the disk disperses, which is thought to happen at about the age of UCL/LCC for M stars, the star is free to spin up. We thus now explore the relationship between disks and rotation for the M stars in UCL/LCC.

Figure 16 zooms in on the M stars in the P versus $(V - K_s)_0$ plot for USco, the confident UCL/LCC disks, and the possible

UCL/LCC disks. As discussed in detail in Paper V, the USco plot has a clear pileup of disked stars at ~ 2 days, which we believe to be a signature of disk locking. For the confident disks in UCL/LCC (middle panel), there is a similar very obvious ~ 2 day pileup in the mid-M stars. Using a two-dimensional two-sided KS test, the disked and nondisked samples are statistically significantly different from each other in the first two panels of Figure 16.

Few disked M stars are found to rotate faster than ~ 2 days in USco (first panel; only 3% of the disked stars have $P < 1$ day,

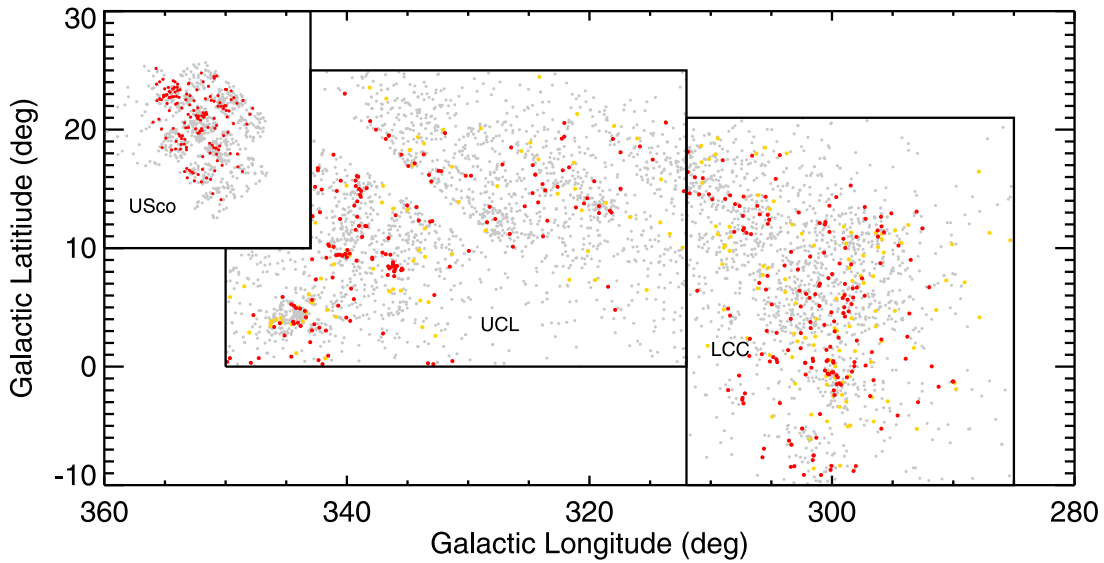


Figure 15. The locations of the targets in Galactic coordinates, as in Figure 1. Stars with high-confidence disks from UCL/LCC (or USco; Paper IV) are marked with red points; stars with lower-confidence disks from UCL/LCC are marked with yellow points. The gray points are simply stars with LCs. The high-confidence disks are clustered, but not nearly as much as they were in USco. The high-confidence disk fractions in both UCL and LCC are $\sim 7\%$ – 8% , and there is no obvious large-scale gradient in disk fraction with position among UCL/LCC.

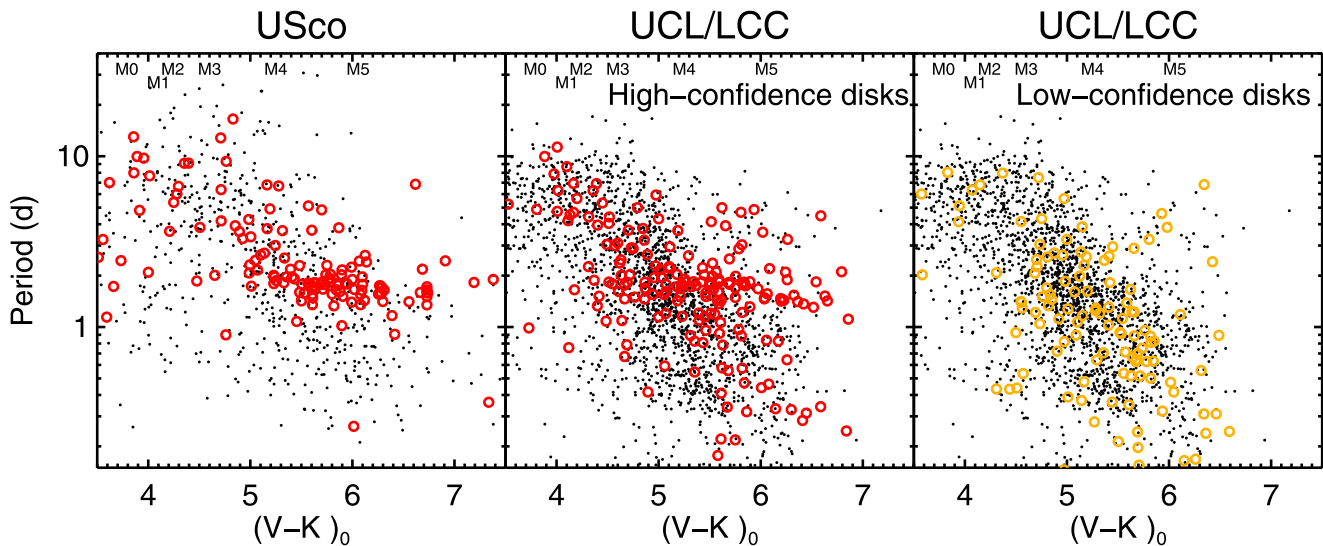


Figure 16. P (in days) vs. $(V - K_s)_0$ for M stars from the gold member sample, where the black points are disk-free M stars, the red circles are high-confidence disked M stars, and the yellow circles are lower-confidence disked M stars. The left panel is USco, and the other two panels are UCL/LCC (the black dots are the same in the middle and right panels). The disked stars have an obvious “pileup” near 2 days among the M stars, and there may be a slope to that 2 day pileup; see the text. The lack of structure in the last panel reinforces our lack of confidence in those disks in general.

compared to 26% of the nondisked stars). However, there are more disked stars rotating faster than ~ 2 days in UCL/LCC (middle panel; 20% of the disked stars have $P < 1$ day, compared to 32% of the nondisked stars). It is not immediately obvious why this would be the case. Since source confusion is an important concern, this is perhaps the most likely reason, meaning largely TESS confusion, but also possibly confusion in WISE. These stars could be fast-rotating because they are binaries, but they do not appear to be photometric binaries in an optical color–magnitude diagram, nor are they in general those stars with multiple periods (in K2, we found that, in particular, M stars with multiple periods were also often photometric binaries).

Figure 17 shows the WISE IR excess $([3.4] - [12])_{\text{observed}} - ([3.4] - [12])_{\text{expected}}$ as a function of P for bins in $(V - K_s)_0$. It

is straightforward to see that the fast-rotating disked stars do not, in general, have multiple periods, nor are they the stars with the larger $12 \mu\text{m}$ IR excesses. A handful of these stars do have secondary periods that are > 1 day, or have discarded periods that are > 1 day. Followup observations of these targets are warranted. It is still the case, as it is for USco, that UCL/LCC stars with disks tend to rotate more slowly than the ensemble. Alternatively, fast-rotating stars tend not to have disks.

There are enough stars in this UCL/LCC member sample that we can break down the distribution into relatively fine bins of $(V - K_s)_0$, and investigate a relationship that was hinted at in USco. In Figure 16, in both USco and UCL/LCC, the pileups at $(V - K_s)_0 \sim 5\text{--}6$ and ~ 2 days seem to have downward slopes. Figure 17 attempts to explore this further;

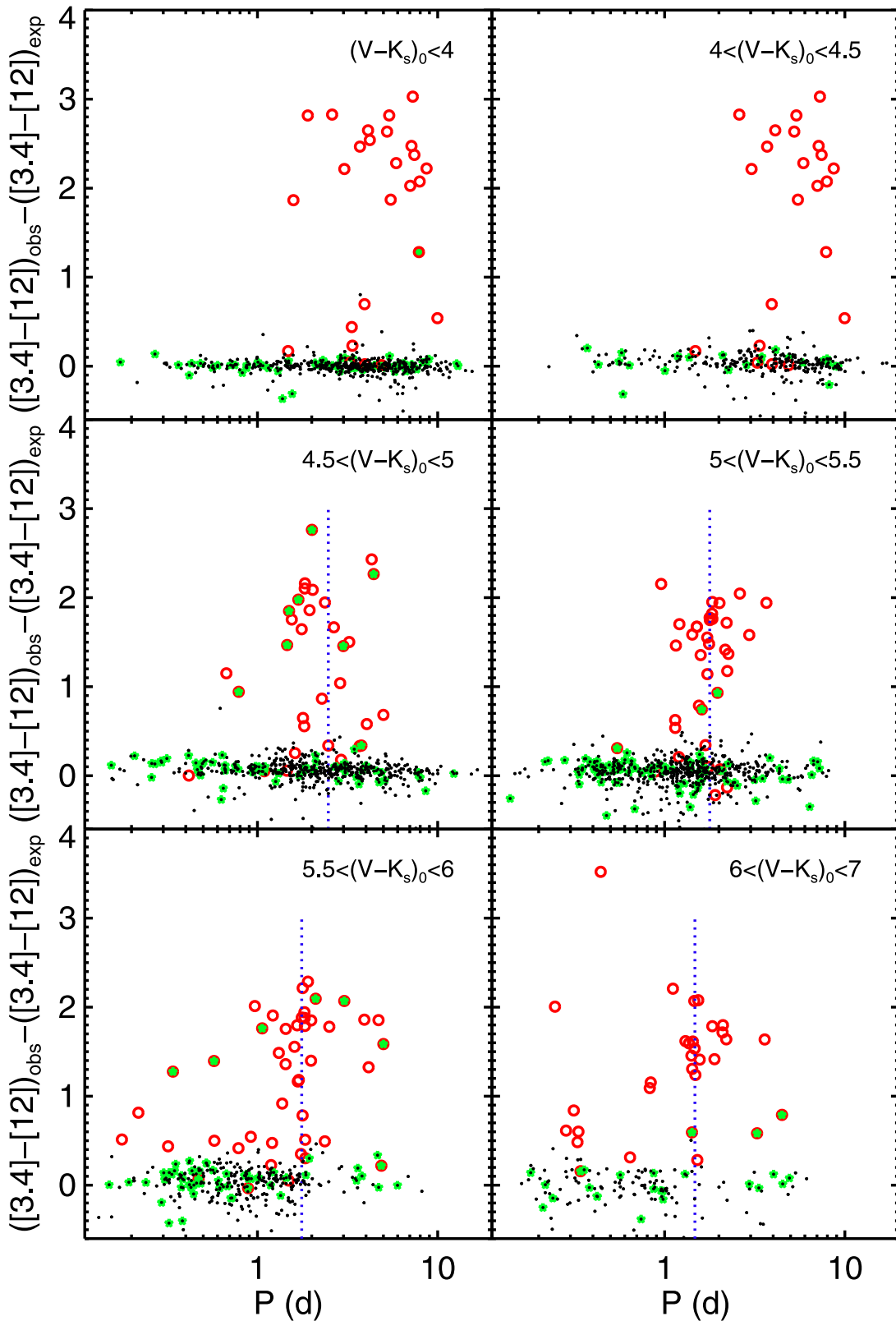


Figure 17. WISE IR excess (observed – expected $[3.4]-[12]$) for gold member stars unlikely to be pulsators, in bins of $(V - K_s)_0$, as shown in each panel. The black dots are stars without disks; the red circles are stars with high-confidence disks. An additional green symbol means that there are multiple periods associated with the object, e.g., it could be a multiple or subject to source confusion. UCL/LCC stars with disks tend to rotate more slowly than the ensemble, or, rather, fast-rotating stars tend not to have disks. The blue vertical dotted lines in the bottom four panels are located at the mean period for disked stars with $(V - K_s)_0 > 4.5$ and $([3.4] - [12])_{\text{observed}} - ([3.4] - [12])_{\text{expected}} > 0.3$ in each panel (2.5, 1.8, 1.8, and 1.5 days, respectively). Among the disked mid-M stars with large IR excesses, M5 stars rotate faster than M3 stars.

for stars with $(V - K_s)_0 > 4.5$, it shows the mean P calculated for disked stars with $([3.4] - [12])_{\text{observed}} - ([3.4] - [12])_{\text{expected}} > 0.3$ in each panel. The M3 stars have a mean P near 2.5 days, and the M5 stars are near 1.5 days, suggesting that among the disked stars with large IR excesses, less massive stars are rotating faster.

The discussion of Figure 12 above noted that the distribution of disk-free UCL/LCC M stars was very sharply peaked at $P \sim 1.5$ days, which is quite close to the pileup of the M-star disked stars at ~ 1.5 – 1.8 days. We speculate whether this clump consists of stars that have shed their dust disks relatively recently and therefore unlocked from their disks, but have not yet had the time to spin up in response, a process that may take a few million years (e.g., Roquette et al. 2021).

We note that the last panel in Figure 16 has very little structure reminiscent of any of the structure seen in the other panels, reinforcing our lack of confidence in those stars having believable disks.

7. Summary and Conclusions

We have presented space-based spot-modulated rotation rates from TESS for $\sim 90\%$ of ~ 3700 UCL/LCC members ($\sim 91\%$ of the ~ 3000 most likely members).

We started from a set of members assembled in the literature largely from Gaia DR2 analyses. We winnowed down the sample, based on what supporting data we could find, whether or not we could obtain a TESS LC, and whether or not that TESS LC could reliably be tied to that source. Based on the available information, we placed the stars into three member bins: gold (the overwhelming majority of the members), silver, and bronze. We also kept track of the sources rejected as members. We identified IR excesses from any available IR band, but WISE-3 ($12 \mu\text{m}$) was the most widely available band, which we used for plotting purposes.

We identified periods in the TESS LCs that compare well with those in the literature, up to ~ 15 days or half a TESS campaign duration. We find periods for $\sim 90\%$ of the UCL/LCC members, with $>60\%$ of those being sinusoidal periods, or close to it, and interpreted them as arising from spots or spot groups that rotate into and out of view. We find a similar variety of LC and periodogram types as we found in our K2 work, but we found a lower fraction of stars with multiple periods. This could be a result of the noise characteristics of the TESS LCs, but it could also be a result of the target selection. Most of the targets were identified based on Gaia selection, which can select against multiplicity. In our K2 work, we found that multiperiod stars, especially among the Ms, were often photometric binaries. Thus, if our input target list was biased against multiples, it makes sense that our sample would be less likely to find multiperiod stars. However, the noise characteristics of the TESS LCs are indeed very different than K2, so that cannot be entirely dismissed as a cause for finding fewer multiperiod stars.

We find more of the scallop shells, flux dips, and transient flux dips initially identified in Stauffer et al. (2017, 2018a, 2018b). Fractionally, we find them at a rate of 3% in the UCL/LCC sample, which is quite consistent, given the relative ages, with 1% of the Pleiades sample, 3% of the USco sample, and 4% of the Taurus sample.

The distribution of P versus $(V - K_s)_0$ color, as a proxy for mass, reveals that UCL/LCC fits in well with evolutionary expectations, given its age. Figures 12 and 14 both show that

the highest and lowest masses probed here are among the fastest rotators; the slowest rotators are in the middle masses. The higher masses are not as “organized” as they presumably will be by the Pleiades age, but, at the same time, they are not as “disorganized” as they presumably were at the USco age. The M stars are already well organized, and follow the same slope as is found in both USco and the Pleiades.

The disk fraction in UCL/LCC is a few percent, and, as a result, there are some disk-influenced LCs—we find both bursters and dippers among the disked stars. The disked M stars form a very obvious pileup at about 2 days in the P versus $(V - K_s)_0$ plot (Figures 16 and 17), a pileup that seems to drift slightly longer as the mass decreases. Interestingly, the distribution of disk-free M stars is also sharply peaked at ~ 2 days, at the same location as the disked stars, suggesting that perhaps these stars have just freed themselves from their disks, but have not yet had the time to react yet.

Some of the data presented in this paper were obtained from the Mikulski Archive for Space Telescopes (MAST). Support for MAST for non-HST data is provided by the NASA Office of Space Science via grant NNX09AF08G and by other grants and contracts. This paper includes data collected by the TESS mission. Funding for the TESS mission is provided by the NASA Explorer Program. This research has made use of the NASA/IPAC Infrared Science Archive (IRSA), which is operated by the Jet Propulsion Laboratory, California Institute of Technology, under contract with the National Aeronautics and Space Administration. This research has made use of NASA’s Astrophysics Data System (ADS) Abstract Service, and of the SIMBAD database, operated at CDS, Strasbourg, France. This research has made use of the VizieR catalog access tool, CDS, Strasbourg, France (DOI: 10.26093/cds/vizieR). The original description of the VizieR service was published in 2000, A&AS 143, 23. This research has made use of data products from the Two Micron All-Sky Survey (2MASS), which is a joint project of the University of Massachusetts and the Infrared Processing and Analysis Center, funded by the National Aeronautics and Space Administration and the National Science Foundation. The 2MASS data are served by the NASA/IPAC Infrared Science Archive, which is operated by the Jet Propulsion Laboratory, California Institute of Technology, under contract with the National Aeronautics and Space Administration. This publication makes use of data products from the Wide-field Infrared Survey Explorer, which is a joint project of the University of California, Los Angeles, and the Jet Propulsion Laboratory/California Institute of Technology, funded by the National Aeronautics and Space Administration.

Facilities: K2, 2MASS, WISE, IRSA, Exoplanet Archive.

Appendix A Rejected/Discarded Sources

As mentioned in detail in the main body of the paper, there are sources that we have discarded from the analysis above for any of a number of reasons, ranging from not having a TESS LC at all or not having a TESS LC that was uncontaminated, to not having a V or a K_s , or other reasons. This appendix largely consists of the table of values for these discarded sources, should later investigators wish to use any of this information. Note that the periods are right for the LCs that we have, but the LCs often do not correspond to the stars listed here; the most

Table 3
Contents of Table: Periods and Supporting Data for Discarded/Rejected Sources

| Number | Label | Contents |
|--------|----------------|---|
| 1 | TIC | Number in the TIC |
| 2 | Name | Coordinate-based (R.A. and decl., J2000) name for target |
| 3 | othername | Alternate name for target |
| 4 | gaiaid | Gaia DR2 ID |
| 5 | distance | Distance from Bailer-Jones et al. (2018) in parsecs |
| 6 | Kmag | K_s magnitude (in Vega mags), if observed |
| 7 | vmk-used | $(V - K_s)$ used, in Vega mags (observed or inferred; see text) |
| 8 | evmk | $E(V - K_s)$ adopted for this star (in mags; see Section 3.3) |
| 9 | Kmag0 | Dereddened $K_{s,0}$ magnitude (in Vega mags), as inferred (see Section 3.3) |
| 10 | vmk0 | $(V - K_s)_0$, dereddened $V - K_s$ (in Vega mags), as inferred (see Section 3.3; rounded to nearest 0.1 to emphasize the relatively low accuracy). |
| 11 | r_vmk-used | Source of $(V - K_s)$ (see Section 3.1): 1= V measured directly from the literature (including SIMBAD), and K_s from 2MASS; 2= V from the literature (see Section 3.1), and K_s from 2MASS; 3= $(V - K_s)$ inferred from Gaia DR1, and G and K_s from 2MASS (see Section 3.1); 4= $(V - K_s)$ inferred from Pan-STARRS1, and G and K_s from 2MASS (see Section 3.1); 6= V inferred from well-populated optical SED, and K_s from 2MASS (see Section 3.1); 7= $(V - K_s)$ inferred from Gaia DR2, and G and K_s from 2MASS (see Section 3.1); -9=no measure of $(V - K_s)$. |
| 12 | r_evmk | Source of $E(V - K_s)$ leading to $(V - K_s)_0$ (see Section 3.3): 1=dereddening from JHK_s diagram (see Section 3.3); 2=dereddening back to $(V - K_s)_0$ expected for spectral type; 3=dereddening from SED fits; 4=used median $E(V - K_s)=0$ (see Section 3.3); -9=no measure of $E(V - K_s)$. |
| 13 | P1 | Primary period, in days (taken to be the rotation period in cases where there is > 1 period) |
| 14 | P2 | Secondary period, in days |
| 15 | P3 | Tertiary period, in days |
| 16 | P4 | Quaternary period, in days |
| 17 | p-uncertcode | Uncertainty code for period—is there any reason to worry about this period? Values are “n” (no worry, full confidence; by far the most common value), “(n)” (no period), with “n?” and “y?” being progressively less confident periods. |
| 18 | IRexcess | Whether an IR excess is present or not (see Section 3.4) |
| 19 | IRexcessStart | The minimum wavelength at which the IR excess is detected or the limit of our knowledge of where there is no excess (see Section 3.4) |
| 20 | SEDslope | Best-fit slope to all detections between 2 and 25 microns |
| 21 | SEDclass | SED class (I, flat, II, or III), based on the SED slope between 2 and 25 microns |
| 22 | dipper | LC matches dipper characteristics (see Section 4.5) |
| 23 | burster | LC matches burster characteristics (see Section 4.5) |
| 24 | single/multi-P | Single or multiperiod star |
| 25 | dd | The LC and power spectrum match double-dip characteristics (see Section 4.5) |
| 26 | ddmoving | The LC and power spectrum match moving double-dip characteristics (see Section 4.5) |
| 27 | shapechanger | LC matches shape changer characteristics (see Section 4.5) |
| 28 | beater | LC has beating visible (see Section 4.5) |
| 29 | complexpeak | The power spectrum has a complex, structured peak and/or has a wide peak (see Section 4.5) |
| 30 | resolvedclose | The power spectrum has resolved close peaks (see Section 4.5) |
| 31 | resolveddist | The power spectrum has resolved distant peaks (see Section 4.5) |
| 32 | pulsator | The power spectrum and LC match pulsator characteristics (see Section 4.5) |
| 33 | scallop | LC matches scallop or flux dip characteristics (see Section 4.5 and Appendix C) |
| 34 | EB | LC has characteristics of eclipsing binary (see Section 4.5 and Appendix C) |

(This table is available in its entirety in machine-readable form.)

common reason we have for rejecting a source is that there is obvious source confusion in the TESS LCs.

Appendix B Comparison to Literature Periods

Section 4.4 discussed in broad terms the comparison of our period-finding to that from the literature. In this appendix, we list the periods for ~ 600 specific stars in common between our study and several literature studies, regardless of whether or not the stars are currently thought to be UCL/LCC members or not. The stars are listed in Table 4. If the TESS period matches the literature period within 15%, we take it as a match. If the TESS period is a match between 15% and 20%, we take it as close, but not quite a match. Several periods are too long for TESS to have recovered. In a few cases, the literature period matches a provisional period identified in TESS or in the literature; in some additional cases, there is a peak in TESS at or near the literature P , but we had discarded the TESS P as being unlikely to be astrophysical and/or more likely to be a timescale than a rotation period. See the notes in the table.

Table 4
Contents of Table: Comparison to Literature Periods

| Number | Label | Contents |
|--------|---------|---|
| 1 | TIC | TIC number |
| 2 | Name | Position-based catalog number |
| 3 | pkiraga | P in days from Kiraga (2012) |
| 4 | pmellon | P in days from Mellon et al. (2017) |
| 5 | pgdr2 | P in days from Gaia DR2 |
| 6 | pasasn | P in days from ASAS-SN |
| 7 | plit | P in days from elsewhere in the literature |
| 8 | r_cite | Citation for literature source of P in column 7 |
| 9 | P1 | First period reported here |
| 10 | P2 | Second period reported here |
| 11 | P3 | Third period reported here |
| 12 | P4 | Fourth period reported here |
| 13 | match | Is this a match? |
| 14 | notes | Notes |

(This table is available in its entirety in machine-readable form.)

Appendix C Unusual LCs

As discussed in Section 4.5, most of the LCs considered here are well behaved, e.g., sinusoidal and clearly periodic (or clearly not), and the periodic signal is easily interpreted as the rotation of the star. However, there are ~ 150 stars ($< 4\%$ of the entire sample) that we wanted to call out here because they are unusual in some way. They are all listed in Table 5, with notes as to why they merited listing here. The parameters for all of them (including periods) are listed in the big data tables above; this table here largely provides notes on these stars. The table includes the TIC number, coordinate-based name, what member sample they are in (gold, silver, bronze, or reject), how confident we are that they should be in the category that we have placed them in (e.g., scallop or EB, etc.) and whether or not the detected period is due to rotation, and any additional notes about them. In the context of the entire sample (or the entire member sample), there are very few LCs for which we are not confident about the bins in which we have placed them, and errors in their categorization do not affect any of our conclusions. A more detailed statistical characterization of any of these stars or categories is beyond the scope of the present paper, so they are simply listed here.

This list includes the scallops and flux dips published in Stauffer et al. (2021), two of which have had to be rejected here, due to source confusion; it also includes new scallops and flux dips identified here, as well as stars that may be scallops or flux dips, but are at lower S/N.

Also in the table are candidate pulsators, including some that have phased waveforms that resemble a “ski jump”—e.g., they look like those of RR Lyr, but these are, in general, very fast (hours). For the pulsators, note that their periods appear in the tables above, but they are omitted from the plots involving P_{rot} , since they are not rotation.

Many obvious EBs appear in the LCs; some phased LCs could be EBs or could be flux dips, and it is very hard to determine from the available (often low-S/N) LC which one it is. In cases of obvious EBs, we have omitted P_{EB} from the plots, but have retained P_{rot} , where it was possible to derive a plausible rotation period estimate from the LC. Of the EBs, about half of them appear above the main sequence, e.g., consistent with being a binary, in Figure 9.

Table 5
List of Unusual Objects

| TIC | Name | Member Bin | Sample Confidence ^a | Notes |
|-----------|--------------------|------------|--------------------------------|---|
| 405235910 | 102115.42-622604.3 | gold | high but not rotation | Pulsator |
| 93952051 | 102646.51-595526.8 | silver | low but not rotation | Pulsator? |
| 273703001 | 103137.10-690158.7 | bronze | high but not rotation | Pulsator |
| 412006082 | 103341.80-641345.7 | gold | high but not rotation | Pulsator |
| 242558208 | 103422.70-641809.3 | silver | high but not rotation | Pulsator |
| 351521478 | 103819.04-612100.7 | silver | high but not rotation | Pulsator |
| 390470134 | 103844.36-595443.7 | silver | high but not rotation | Pulsator |
| 419686932 | 104122.99-694043.1 | silver | high but not rotation | Pulsator |
| 92574021 | 113249.19-494907.8 | gold | low | Scallop? |
| 451984338 | 113319.04-594822.0 | gold | high but not rotation | EB, only P is that of binary; $P_{EB}=1.132$. |
| 290889135 | 113556.21-653012.1 | gold | high | Scallop in p2. |
| 280945693 | 113616.71-692751.8 | gold | high | Published as flux dip in Stauffer+21. |
| 452345586 | 113658.55-582237.5 | gold | high | Flux dip |
| 93763678 | 114322.41-532711.4 | gold | high | Flux dip |
| 323478101 | 114557.95-635246.3 | gold | high but not rotation | EB, only P is that of binary; $P_{EB}=0.477$. |
| 296790810 | 114625.66-664135.6 | gold | high | Published as flux dip in Stauffer+21; possible small IR excess. |
| 268665785 | 114902.67-570014.1 | gold | low | Possible EB; extracted P_{rot} . |
| 301432612 | 115404.70-580241.3 | gold | high | Published as scallop in Stauffer+21. |
| 307686978 | 120017.79-635549.0 | bronze | high | EB, but can pull out P_{rot} ; $P_{EB}=2.778$. |
| 398768350 | 120119.80-564902.7 | gold | high | Published as scallop in Stauffer+21. |
| 379774242 | 120504.18-644721.6 | gold | low | Scallop? |
| 994964114 | 120858.09-513019.6 | reject | (reject) | Source confusion so rejected, but p1 could be a flux dip. |
| 994964138 | 120858.19-513017.2 | reject | (reject) | Source confusion so rejected, but p1 could be a flux dip. |
| 334409011 | 121318.43-515641.6 | gold | high | EB, but can pull out P_{rot} ; $P_{EB}=3.361$. |
| 288093002 | 122028.00-543537.6 | gold | high | Published as flux dip in Stauffer+21. |
| 310412874 | 122048.65-640904.1 | silver | low | Flux dip? Small IR excess. |
| 448002486 | 122138.04-690838.4 | gold | high | Published as flux dip in Stauffer+21. |
| 310720311 | 122153.09-634733.9 | gold | high | Published as scallop in Stauffer+21. |
| 411614400 | 122201.40-573757.1 | gold | high but not rotation | EB, only P is that of binary; $P_{EB}=1.535$. |
| 135162879 | 122213.16-414802.7 | gold | high | Published as scallop in Stauffer+21. |
| 311447879 | 122220.20-650950.6 | bronze | low | Flux dip? |
| 311333943 | 122247.22-633757.6 | silver | low | Flux dip, possible IR excess, possible icicles? |
| 261573174 | 122303.08-542526.9 | silver | low | Possible EB; extracted P_{rot} ; $P_{EB}=1.084$. |
| 311592558 | 122348.30-633248.7 | silver | low | Possible EB; extracted P_{rot} . |
| 311585720 | 122354.75-641730.0 | silver | high but not rotation | EB, only P is that of binary; $P_{EB}=0.612$. |
| 450386147 | 122424.02-645344.0 | gold | low | Flux dip? |
| 273460357 | 122500.61-521627.1 | reject | (reject) | Source confusion so rejected, but an interesting LC shape. |
| 273460338 | 122501.42-521614.6 | reject | (reject) | Source confusion so rejected, but an interesting LC shape. |
| 281742840 | 122504.80-655942.1 | bronze | high but not rotation | EB, only P is that of binary; $P_{EB}=4.760$. |
| 271221172 | 122657.75-554620.0 | gold | high but not rotation | EB, only P is that of binary; $P_{EB}=0.266$. |
| 450957950 | 122902.23-645500.6 | gold | high but not rotation | EB, only P is that of binary; $P_{EB}=2.360$. |
| 272407484 | 123108.44-545644.5 | gold | low | Flux dip in p2; clear IR excess. |
| 179968331 | 123410.56-635241.6 | gold | high but not rotation | EB, only P is that of binary; $P_{EB}=2.825$. |
| 273821594 | 123624.97-550710.6 | gold | high | Scallop and flux dip? |
| 411681763 | 123742.99-554851.2 | gold | high but not rotation | EB, only P is that of binary; $P_{EB}=1.415$. |
| 73183013 | 123941.30-464444.6 | gold | high | Three dips per cycle, still sinusoidal. |
| 161734785 | 124147.22-511006.7 | gold | high | Published as scallop in Stauffer+21. |

Table 5
(Continued)

| TIC | Name | Member Bin | Sample Confidence ^a | Notes |
|-----------|--------------------|------------|--------------------------------|---|
| 412182239 | 124231.62-590512.6 | silver | low | Two very clear v-shaped dips per cycle, not evenly spaced. Substantial IR excess and long P (1.3 days), both of which are inconsistent with scallop category. Counted as scallop, but...? |
| 328468855 | 124301.62-675620.8 | gold | high | Flux dip |
| 419502814 | 124434.42-551246.5 | gold | high | EB, but can pull out P_{rot} ; $P_{\text{EB}}=1.059$. |
| 419779703 | 124631.20-540431.4 | gold | high | Scallop |
| 405695928 | 124826.12-553816.1 | silver | high | Flux dip |
| 405754448 | 124831.44-594449.8 | gold | low | Scallop shape, but at $(V - K_s)_0 \sim 3$ —this is too blue for a scallop; and at $P \sim 0.5$, it is much faster than other stars of its color. Source confusion? |
| 165904363 | 124942.09-495316.3 | gold | high | Flux dip |
| 165912675 | 125033.96-482656.5 | gold | low | Flux dip? |
| 405970436 | 125058.63-593400.6 | gold | high | Scallop |
| 405910532 | 125100.26-564313.1 | reject | (reject) | Source confusion so rejected, but could be EB. |
| 405910546 | 125100.61-564321.0 | reject | (reject) | Source confusion so rejected, but could be EB. |
| 412376751 | 125129.47-592421.7 | gold | low | Flux dip? |
| 412376096 | 125137.68-592945.0 | bronze | high | Flux dip |
| 435899024 | 125222.75-641839.4 | gold | high | Published as scallop in Stauffer+21; possible IR excess. |
| 406040223 | 125521.95-584641.8 | gold | high | Published as flux dip in Stauffer+21. |
| 248145126 | 125545.32-445151.7 | gold | high | Published as scallop in Stauffer+21; possible IR excess. |
| 335598085 | 125935.63-680801.6 | gold | high | Published as scallop in Stauffer+21. |
| 253239639 | 130159.57-592023.8 | gold | high but not rotation | “Ski jump”; shaped like RR Lyr, but very fast. |
| 404335106 | 130317.73-515013.0 | gold | low | Flux dip, though at ~ 3 days, the period is very long compared to other flux dips. |
| 404387832 | 130354.33-501502.3 | gold | high | Scallop |
| 439883940 | 130416.15-640557.0 | silver | high | EB, but can pull out P_{rot} ; $P_{\text{EB}}=6.176$. |
| 258583707 | 130730.60-454919.7 | gold | low | Flux dip? EB? Counted as flux dip. |
| 441263248 | 130927.70-653325.5 | gold | high | EB, but can pull out P_{rot} ; $P_{\text{EB}}=6.877$. |
| 245002119 | 130949.27-513546.3 | gold | high but not rotation | EB, only P is that of binary; $P_{\text{EB}}=0.581$. |
| 363656704 | 131920.44-450800.7 | gold | high | EB, but can pull out P_{rot} . |
| 973449111 | 131935.91-623436.9 | gold | high | Published as flux dip in Stauffer+21. |
| 438709950 | 132424.75-475730.1 | gold | low | Flux dip? |
| 243192504 | 133157.69-470614.9 | gold | high | EB, but can pull out P_{rot} . |
| 261272259 | 133521.22-493921.0 | bronze | high | EB? Dominant P is P_{rot} , with eclipses. |
| 241375625 | 133852.06-510507.0 | gold | high | Flux dip in p2. |
| 243381460 | 134001.65-434857.3 | gold | high | Published as scallop in Stauffer+21. |
| 243449997 | 134233.80-460826.4 | gold | high | Flux dip |
| 243499565 | 134435.82-470613.8 | gold | high | Published as flux dip in Stauffer+21. |
| 166302995 | 134518.06-410202.2 | gold | low | Possible EB; extracted P_{rot} ; $P_{\text{EB}}=2.881$. |
| 207621404 | 134732.79-553301.9 | gold | high | Published as scallop in Stauffer+21. |
| 243611773 | 134816.29-440238.8 | gold | high | Published as flux dip in Stauffer+21; flux dip in p2. |
| 208351772 | 135345.11-554420.0 | silver | high | EB, but can pull out P_{rot} ; $P_{\text{EB}}=5.003$. |
| 448165364 | 135407.42-673344.9 | gold | high | Three dips per cycle, still sinusoidal. |
| 312410638 | 140146.25-501537.3 | gold | high | Flux dip |
| 328906141 | 140554.60-522600.5 | gold | high | Published as scallop in Stauffer+21. |
| 179368022 | 140729.83-385427.0 | gold | high | Scallop in p2. |
| 179367270 | 140731.25-393216.8 | gold | high | Flux dip, though at ~ 3 days, the period is very long compared to other flux dips. |
| 329694185 | 140953.34-521717.7 | silver | high | Scallop |
| 330560000 | 141424.51-510319.3 | gold | high | Published as flux dip in Stauffer+21. |
| 242407571 | 141424.86-455643.6 | gold | high | Published as scallop in Stauffer+21; noted as having second period that manifests as “icicles.” |

Table 5
(Continued)

| TIC | Name | Member Bin | Sample Confidence ^a | Notes |
|------------|--------------------|------------|--------------------------------|---|
| 330791148 | 141529.27-495747.5 | gold | high | EB? Can pull out P_{rot} ; $P_{\text{EB}}=3.430$. |
| 448852739 | 141605.67-691735.8 | gold | high | EB, but can pull out P_{rot} . |
| 167448346 | 142229.54-385517.1 | gold | high but not rotation | EB, only P is that of binary; $P_{\text{EB}}=0.548$. |
| 242594123 | 142347.41-432457.3 | gold | high but not rotation | EB, only P is that of binary; $P_{\text{EB}}=2.548$. |
| 241841997 | 142758.40-392328.7 | gold | low | Scallop in p3, or possible EB. P3 is <0.5 days, so counted as scallop. |
| 127309526 | 142759.62-432629.2 | gold | high | Published as flux dip in Stauffer+21; flux dip in p2. |
| 211513644 | 142809.56-491545.9 | gold | high | Published as flux dip in Stauffer+21. |
| 127246012 | 142829.78-455715.4 | gold | high | Scallop |
| 241884143 | 143112.81-410358.6 | gold | low | Could be flux dip in p2, could be EB. High enough in color–magnitude diagram to be photometric binary. Counted as flux dip. |
| 127866051 | 143333.84-474354.5 | silver | high | Scallop |
| 159427926 | 143958.40-402809.3 | reject | (reject) | Source confusion so rejected, but p1 is a flux dip. |
| 159427927 | 143958.71-402809.4 | reject | (reject) | Source confusion so rejected, but p1 is a flux dip. |
| 129116176 | 144134.97-470029.3 | gold | high but not rotation | EB, only P is that of binary; $P_{\text{EB}}=2.023$. |
| 129116164 | 144139.29-470015.1 | silver | high but not rotation | EB, only P is that of binary; $P_{\text{EB}}=2.019$. |
| 129309458 | 144343.05-433756.0 | gold | high | Flux dip |
| 309321971 | 145537.81-493427.7 | gold | high | Scallop |
| 461643692 | 145823.13-334415.4 | gold | high | Published as flux dip in Stauffer+21. |
| 334325329 | 150031.41-462131.4 | gold | high | Flux dip |
| 75489110 | 150033.42-342954.6 | gold | high but not rotation | “Ski jump” in P2; shaped like RR Lyr, but very fast. |
| 334838280 | 150234.31-441933.2 | gold | low | Flux dip? |
| 121727134 | 150455.33-375746.9 | gold | high but not rotation | EB, contact binary, only P is that of binary; $P_{\text{EB}}=0.374$. |
| 121840452 | 150516.87-381412.4 | gold | high | Published as scallop in Stauffer+21. |
| 366178112 | 150638.97-435728.9 | gold | low | Possible “ski jump”? Or flux dip? Unclear. |
| 160539036 | 150757.83-440458.7 | gold | low | Flux dip in p2. |
| 76048114 | 150804.78-314231.8 | reject | (reject) | Source confusion so rejected, but p2 is a scallop. |
| 76048113 | 150805.11-314231.4 | reject | (reject) | Source confusion so rejected, but p2 is a scallop. |
| 140765939 | 151339.89-434020.8 | gold | high | Flux dip |
| 276502773 | 151433.88-405419.8 | silver | high | Scallop |
| 76698847 | 151616.51-322309.6 | gold | high | Flux dip |
| 148218929 | 151858.60-374518.5 | gold | high but not rotation | EB, only P is that of binary; $P_{\text{EB}}=1.768$. |
| 272398365 | 151903.08-321453.9 | gold | high | Flux dip |
| 89026133 | 152234.45-350414.6 | reject | (reject) | Published as flux dip in Stauffer+21; possible IR excess; now have to reject for source confusion. |
| 89026136 | 152235.51-350357.7 | reject | (reject) | Published as flux dip in Stauffer+21; possible IR excess; now have to reject for source confusion. |
| 147828926 | 152257.19-455619.2 | gold | high | Scallop |
| 173267960 | 153758.40-403805.3 | gold | high | Flux dip in p3. |
| 176205621 | 154212.72-410955.5 | gold | high | Flux dip |
| 177906792 | 154426.96-362543.2 | gold | low | Scallop in p2. |
| 254612758 | 154508.33-442607.9 | gold | high | Published as flux dip in Stauffer+21. |
| 99207324 | 154606.01-352510.7 | gold | high | Published as flux dip in Stauffer+21. |
| 179357494 | 154713.17-411451.1 | gold | low | Flux dip? |
| 442575691 | 154802.96-305431.8 | gold | low | Scallop? |
| 364291454 | 155607.07-400036.2 | gold | low | P1 is “ski jump” (shaped like RR Lyr, but very fast); p2 is flux dip. |
| 1172201258 | 155709.59-320434.2 | reject | (reject) | Source confusion so rejected, but p1 is a flux dip. |
| 1172201260 | 155709.76-320434.3 | reject | (reject) | Source confusion so rejected, but p1 is a flux dip. |
| 58753591 | 155758.97-415846.6 | gold | high but not rotation | “Ski jump”; shaped like RR Lyr, but very fast. |
| 279691401 | 155915.83-365712.3 | gold | high but not rotation | “Ski jump”; shaped like RR Lyr, but very fast. |
| 69874547 | 160556.03-373748.2 | silver | high but not rotation | EB, only P is that of binary; $P_{\text{EB}}=0.795$. |

Table 5
(Continued)

| TIC | Name | Member Bin | Sample Confidence ^a | Notes |
|-----------|--------------------|------------|--------------------------------|---|
| 4231194 | 162231.10-410527.8 | gold | low | Possible EB; $P_{EB}=0.284$. |
| 223461868 | 162508.50-415446.5 | silver | high | EB, but can pull out P_{rot} ; $P_{EB}=1.325$. |
| 84187344 | 163854.75-405519.8 | silver | low | Flux dip? “icicle”? ~ 4 day period too long for flux dip, but does not look like EB. |
| 84756561 | 163952.56-394431.1 | gold | high but not rotation | EB, contact binary, only P is that of binary; $P_{EB}=0.449$. |
| 85125492 | 164033.61-390722.1 | gold | low | Flux dip? Blue $((V - K_s)_0 \sim 4)$ for a flux dip, and has a significant IR excess. |
| 85356121 | 164116.54-382322.8 | gold | low | Flux dip? |
| 77919426 | 164400.33-395943.8 | gold | high but not rotation | EB, only P is that of binary; $P_{EB}=1.333$. |
| 96140771 | 164455.86-341043.3 | gold | high | EB, but can pull out P_{rot} ; $P_{EB}=1.290$. |
| 97239026 | 164717.49-324535.8 | gold | low | Scallop? |
| 337253450 | 165043.59-371212.9 | gold | high | EB, but can pull out P_{rot} ; $P_{EB}=1.927$. |
| 337243787 | 165050.98-381226.5 | gold | low | Flux dip |
| 191694822 | 165108.97-330059.4 | gold | high | EB? Can pull out P_{rot} . |

Note.

^a “Sample confidence” means how confident we are in both the placement in the category (e.g., “scallop” or “EB”) and in the measured period being rotation.

(This table is available in machine-readable form.)

Appendix D

Timescales

Some LCs have some repeated patterns that we cannot identify with certainty as a rotation period. Table 6 summarizes these timescales for the stars from the entire ensemble. Note the

frequent appearance of 6–8 day timescales (or multiples thereof)—this may be a timescale introduced by TESS or the data reduction (see Section 4.3).

Table 6
List of Objects with Timescales

| TIC | Name | Timescale (d) and/or Notes |
|------------|--------------------|--|
| 0311456083 | 122327.67-653614.1 | 2.4? 6.5? |
| 0425319705 | 124406.63-555418.2 | 7.5? |
| 0253309679 | 130350.87-582054.7 | 15? |
| 0253451463 | 130713.28-542732.7 | 6? |
| 0253455154 | 130807.49-543230.9 | 8? |
| 0406246159 | 131022.15-591740.0 | 5? |
| 0253957851 | 131600.11-570415.6 | 6? |
| 0245266758 | 131723.19-512217.4 | 2? 5? 14? Has IR excess |
| 1048575980 | 132507.42-430409.8 | 4? 8? Very close to NGC 5128 (Cen A) |
| 0243222122 | 133408.54-472700.9 | 15? |
| 0243249579 | 133419.83-433250.1 | 4? |
| 0413084801 | 133908.59-585128.6 | 7? |
| 1052983805 | 134132.37-443044.0 | 20? |
| 0275884492 | 135209.38-433223.6 | 4? |
| 0241684780 | 135230.72-515337.2 | 5? 6? |
| 0208317834 | 135324.21-574630.0 | 5? Done on portion of LC |
| 0242153310 | 140108.61-443029.4 | 8? |
| 0329007676 | 140639.03-502509.3 | 5? |
| 0179410344 | 140809.36-391251.5 | 6? |
| 0242548815 | 142119.68-474532.7 | 7? |
| 0180028859 | 142123.18-390714.4 | 7? |
| 0392752922 | 143120.10-350835.6 | 4? |
| 0289425666 | 143749.01-492827.4 | 7.2? |
| 0159656935 | 144223.07-404149.7 | 2? 12? |
| 0159711236 | 144346.08-371908.9 | 3? 0.4? Done on portion of LC |
| 0159751326 | 144426.97-415323.0 | 2? 4? Has IR excess |
| 0451276379 | 144431.39-485707.1 | 451276379 and 451276381 are confused; 4? |
| 0451276381 | 144431.74-485710.3 | 451276379 and 451276381 are confused; 4? |
| 0460218478 | 144911.31-500114.0 | 6? |
| 0335145136 | 150425.51-453050.5 | 7? 11? |
| 0121932858 | 150618.61-412016.9 | 1.3? |
| 0160476756 | 150708.81-445555.0 | 6.4? |
| 0160818175 | 150947.71-461948.4 | 4? |
| 0185053184 | 152803.22-260003.4 | 7? |
| 0054516263 | 152812.46-343606.0 | 5? |
| 0153781950 | 153141.33-472926.2 | 9? 5? |
| 0171609844 | 153538.29-410709.2 | 8? |
| 0172608416 | 153650.92-384138.6 | 5? |
| 0290559990 | 153745.91-423656.8 | 5? 15? |
| 0254394156 | 154034.80-445322.3 | 15? |
| 0178767016 | 154659.81-395344.3 | 7? 12? |
| 0179347980 | 154711.40-392414.4 | 8? |
| 0179058102 | 154723.35-364411.6 | 6? 5? |
| 0442586515 | 154854.12-351319.2 | 7? |
| 0442623945 | 154912.10-353905.5 | 10? Disky LC, and has IR excess |
| 0058245194 | 155302.65-363305.7 | 7? |
| 0058170116 | 155307.05-385500.4 | 7? |
| 0255260454 | 155721.11-433342.9 | 5? |
| 0279883855 | 155916.48-415710.7 | 7? Disky LC, and has IR excess; burster |
| 0059016771 | 155958.21-360255.6 | 12? Matches literature! |
| 0059501088 | 160233.48-362923.4 | 59501088 and 59501092 are confused; 5? |
| 0059501092 | 160233.48-362928.3 | 59501088 and 59501092 are confused; 5? |
| 0257368371 | 160317.74-421502.5 | 5? Has IR excess |
| 0256901758 | 160319.73-442214.2 | 4? |

Table 6
(Continued)

| TIC | Name | Timescale (d) and/or Notes |
|------------|--------------------|--|
| 0069514999 | 160445.05-380512.0 | 3.5? 7? |
| 0457995946 | 160854.69-393743.6 | Disky, 2.4? Has IR excess |
| 0382700580 | 160928.01-384854.2 | 7? |
| 0382714814 | 160942.04-405225.4 | 7? |
| 0164027526 | 161152.32-420436.2 | 2? |
| 0004231380 | 162250.15-410301.2 | 6? |
| 0225431084 | 162828.83-444903.2 | 2? Short-P thing seen by eye, cannot recover |
| 0029459205 | 163121.55-394350.8 | 7? |
| 0291256981 | 163308.67-382215.2 | 8? |
| 0083468373 | 163741.14-370654.4 | 8? |
| 0458060193 | 164156.02-395300.7 | 6? |
| 0458203191 | 164212.49-392611.5 | 7? |
| 0077918101 | 164426.14-400803.6 | 7? |
| 0078874478 | 164619.08-392723.8 | 8? |
| 0337243291 | 165046.65-381526.2 | 2? |

(This table is available in machine-readable form.)

ORCID iDs

L. M. Rebull  <https://orcid.org/0000-0001-6381-515X>
 J. R. Stauffer  <https://orcid.org/0000-0003-3595-7382>
 A. M. Cody  <https://orcid.org/0000-0002-3656-6706>
 Ethan Kruse  <https://orcid.org/0000-0002-0493-1342>
 Brian P. Powell  <https://orcid.org/0000-0003-0501-2636>

References

- AKARI team 2010a, AKARI/FIS All-Sky Survey Bright, Source Catalogue, IRSA, doi:[10.26131/IRSA180](https://doi.org/10.26131/IRSA180)
 AKARI Team 2010b, AKARI/IRC Point, Source Catalogue IRSA, doi:[10.26131/IRSA181](https://doi.org/10.26131/IRSA181)
 Akeson, R. L., Chen, X., Ciardi, D., et al. 2013, *PASP*, **125**, 989
 Alfonso-Garzón, J., Domingo, A., Mas-Hesse, J. M., et al. 2012, *A&A*, **548**, A79
 Avallone, E. A., Tayar, J. N., van Saders, J. L., et al. 2022, *ApJ*, **930**, 7
 Bailer-Jones, C. A. L., Rybizki, J., Fouesneau, M., et al. 2018, *AJ*, **156**, 58
 Bailer-Jones, C. A. L., Rybizki, J., Fouesneau, M., et al. 2021, *AJ*, **161**, 147
 Batalha, C. C., Quast, G. R., Torres, C. A. O., et al. 1998, *A&AS*, **128**, 561
 Blaauw, A. 1964, *ARA&A*, **2**, 213
 Bouma, L., Hartman, J., Bhatti, W., Winn, J., & Bakos, G. 2019, *ApJS*, **245**, 13
 Bowler, B. P., Hinkley, S., Ziegler, C., et al. 2019, *ApJ*, **877**, 60
 Broeg, C., Schmidt, T. O. B., Guenther, E., et al. 2007, *A&A*, **468**, 1039
 Burke, C. J., Levine, A., Fausnaugh, M., et al. 2020, 0.4.1, *Astrophysics Source Code Library*, record, [ascl:2003:001](https://arxiv.org/abs/2003.001)
 Capak, P. 2013, Spitzer Enhanced Imaging Products (SEIP) Source List, IRSA, doi:[10.26131/IRSA3](https://doi.org/10.26131/IRSA3)
 Cardelli, J. A., Clayton, G. C., & Mathis, J. S. 1989, *ApJ*, **345**, 245
 Carpenter, J. M., Bouwman, J., Mamajek, E. E., et al. 2009, *ApJS*, **181**, 197
 CatWISE team 2020, CatWISE Preliminary Catalog, IPAC, doi:[10.26131/IRSA126](https://doi.org/10.26131/IRSA126)
 Chambers, K., Magnier, E., Metcalf, N., et al. 2016, arXiv:[1612.05560](https://arxiv.org/abs/1612.05560)
 Chen, C. H., Mittal, T., Kuchner, M., et al. 2014, *ApJS*, **211**, 25
 Christiansen, J. L., Derekas, A., Kiss, L. L., et al. 2008, *MNRAS*, **385**, 1749
 Cody, A. M., & Hillenbrand, L. A. 2018, *AJ*, **156**, 71
 Cody, A. M., Stauffer, J., Baglin, A., et al. 2014, *AJ*, **147**, 82
 Cody, A. M., Hillenbrand, L. A., & Rebull, L. M. 2022, *AJ*, **163**, 212
 Coker, C. T., Pinsonneault, M., & Terndrup, D. M. 2016, *ApJ*, **833**, 122
 Comerón, F., Spezzi, L., & López Martí, B. 2009, *A&A*, **500**, 1045
 Cotten, T. H., & Song, I. 2016, *ApJS*, **225**, 15
 Cruzalèbes, P., Petrov, R. G., Robbe-Dubois, S., et al. 2019, *MNRAS*, **490**, 3158
 Curtis, J. L., Agüeros, M. A., Matt, S. P., et al. 2020, *ApJ*, **904**, 140
 Damiani, F., Prisinzano, L., Pillitteri, I., et al. 2019, *A&A*, **623**, A112
 David, T. J., Hillenbrand, L. A., Gillen, E., et al. 2019, *ApJ*, **872**, 161
 de Zeeuw, P. T., Hoogerwerf, R., de Bruijne, J. H. J., et al. 1999, *AJ*, **117**, 354
 DENIS team 1999, DENIS catalog, IPAC, doi: [10.26131/IRSA478](https://doi.org/10.26131/IRSA478)
 Desidera, S., Covino, E., Messina, S., et al. 2015, *A&A*, **573**, A126
 Distefano, E., Lanzafame, A. C., Lanza, A. F., et al. 2016, *A&A*, **591**, A43
 Donati, J.-F., Gregory, S. G., Alencar, S. H. P., et al. 2012, *MNRAS*, **425**, 2948
 Drake, A. J., Djorgovski, S. G., Catelan, M., et al. 2017, *MNRAS*, **469**, 3688
 Eisenhardt, P. R. M., Marocco, F., Fowler, J. W., et al. 2020, *ApJS*, **247**, 69
 Epchtein, N., Deul, E., Derriere, S., et al. 1999, *A&A*, **349**, 236
 Faherty, J. K., Bochanski, J. J., Gagné, J., et al. 2018, *ApJ*, **863**, 91
 Feinstein, A. D., Montet, B. T., Foreman-Mackey, D., et al. 2019, *PASP*, **131**, 094502
 Fruth, T., Cabrera, J., Chini, R., et al. 2013, *AJ*, **146**, 136
 Gaia Collaboration, Brown, A. G. A., Vallenari, A., et al. 2016a, *A&A*, **595**, A2
 Gaia Collaboration, Brown, A. G. A., Vallenari, A., et al. 2016b, Gaia Catalog DR1, IRSA, doi:[10.26131/IRSA16](https://doi.org/10.26131/IRSA16)
 Gaia Collaboration, Brown, A. G. A., Vallenari, A., et al. 2018a, *A&A*, **616**, A1
 Gaia Collaboration, Brown, A. G. A., Vallenari, A., et al. 2018b, Gaia Source Catalog DR2, doi:[10.26131/IRSA12](https://doi.org/10.26131/IRSA12)
 Gaia Collaboration, Brown, A. G. A., Vallenari, A., et al. 2021, *A&A*, **649**, A1
 Galli, P. A. B., Bertout, C., Teixeira, R., et al. 2015, *A&A*, **580**, A26
 Galli, P. A. B., Bertout, C., Teixeira, R., et al. 2013, *A&A*, **558**, A77
 Ghosh, P., Lamb, F. K., & Pethick, C. J. 1977, *ApJ*, **217**, 578
 Girard, T. M., van Altena, W. F., Zacharias, N., et al. 2011, *AJ*, **142**, 15
 Goldman, B., Röser, S., Schilbach, E., et al. 2018, *ApJ*, **868**, 32
 Günther, M. N., Berardo, D. A., Ducrot, E., et al. 2022, *AJ*, **163**, 144
 Henden, A. A., Templeton, M., Terrell, D., et al. 2016, *yCat*, **II/336**
 Howell, S. B., Sobeck, C., Haas, M., et al. 2014, *PASP*, **126**, 398
 Huang, C. X., Vanderburg, A., Pál, A., et al. 2020a, *RNAAS*, **4**, 204
 Huang, C. X., Vanderburg, A., Pál, A., et al. 2020b, *RNAAS*, **4**, 206
 Indebetouw, R., Mathis, J. S., Babler, B. L., et al. 2005, *ApJ*, **619**, 931
 Jang-Condell, H., Chen, C. H., Mittal, T., et al. 2015, *ApJ*, **808**, 167
 Jayasinghe, T., Kochanek, C. S., Stanek, K. Z., et al. 2018, *MNRAS*, **477**, 3145
 Kapteyn, J. C. 1914, *ApJ*, **40**, 43
 Kerr, R. M. P., Rizzuto, A. C., Kraus, A. L., et al. 2021, *ApJ*, **917**, 23
 Kiraga, M. 2012, *AcA*, **62**, 67
 Koenigl, A. 1991, *ApJL*, **370**, L39
 Kóspál, Á., Mohler-Fischer, M., Sicilia-Aguilar, A., et al. 2014, *A&A*, **561**, A61
 Kounkel, M., & Covey, K. 2019, *AJ*, **158**, 122
 Lasker, B. M., Lattanzi, M. G., McLean, B. J., et al. 2008, *AJ*, **136**, 735
 Luhman, K. L. 2022a, *AJ*, **163**, 25
 Luhman, K. L. 2022b, *AJ*, **163**, 24
 Luhman, K. L., & Mamajek, E. E. 2012, *ApJ*, **758**, 31
 Meisner, A. M., Lang, D., Schlafly, E. F., et al. 2019, *PASP*, **131**, 124504
 Mellon, S. N., Mamajek, E. E., Oberst, T. E., et al. 2017, *ApJ*, **844**, 66
 Messina, S., Desidera, S., Turatto, M., et al. 2010, *A&A*, **520**, A15
 Messina, S., Desidera, S., Lanzafame, A. C., et al. 2011, *A&A*, **532**, A10
 Meyer, M. R., Calvet, N., & Hillenbrand, L. A. 1997, *AJ*, **114**, 288
 Mittal, T., Chen, C. H., Jang-Condell, H., et al. 2015, *ApJ*, **798**, 87

- Moolekamp, F. E., Mamajek, E. E., James, D. J., et al. 2019, *MNRAS*, **484**, 5049
- Murakami, H., Baba, H., Barthel, P., et al. 2007, *PASJ*, **59**, S369
- Nicholson, B. A., Hussain, G. A. J., Donati, J.-F., et al. 2018, *MNRAS*, **480**, 1754
- Pecaut, M. J., Mamajek, E. E., & Bubar, E. J. 2012, *ApJ*, **746**, 154
- Pecaut, M. J., & Mamajek, E. E. 2013, *ApJS*, **208**, 9
- Pecaut, M. J., & Mamajek, E. E. 2016, *MNRAS*, **461**, 794
- Popinchalk, M., Faherty, J. K., Kiman, R., et al. 2021, *ApJ*, **916**, 77
- Rampalli, R., Agüeros, M. A., Curtis, J. L., et al. 2021, *ApJ*, **921**, 167
- Rebull, L. M., Stauffer, J. R., Bouvier, J., et al. 2016a, *AJ*, **152**, 113
- Rebull, L. M., Stauffer, J. R., Bouvier, J., et al. 2016b, *AJ*, **152**, 114
- Rebull, L. M., Stauffer, J. R., Hillenbrand, L. A., et al. 2017, *ApJ*, **839**, 92
- Rebull, L. M., Stauffer, J. R., Cody, A. M., et al. 2018, *AJ*, **155**, 196
- Rebull, L. M., Stauffer, J. R., Cody, A. M., et al. 2020, *AJ*, **159**, 273
- Rebull, L. M., Stauffer, J. R., Cody, A. M., et al. 2021, *AJ*, **162**, 172
- Ribas, Á., Merín, B., Bouy, H., et al. 2014, *A&A*, **561**, A54
- Ribas, Á., Bouy, H., & Merín, B. 2015, *A&A*, **576**, A52
- Ricker, G. R., Winn, J. N., Vanderspek, R., et al. 2015, *JATIS*, **1**, 014003
- Ripepi, V., Molinaro, R., Musella, I., et al. 2019, *A&A*, **625**, A14
- Roquette, J., Matt, S. P., Winter, A. J., Amard, L., & Stasevic, S. 2021, *MNRAS*, **508**, 3710
- Samus', N. N., Kazarovets, E. V., Durlevich, O. V., et al. 2017, *ARep*, **61**, 80
- Scargle, J. D. 1982, *ApJ*, **263**, 835
- Siwak, M., Ogloza, W., Rucinski, S. M., et al. 2016, *MNRAS*, **456**, 3972
- Skiff, B. A. 2014, VizieR On-line Data Catalog (Flagstaff, AZ: Lowell Observatory)
- Skrutskie, M. F., Cutri, R. M., Stiening, R., et al. 2006, *AJ*, **131**, 1163
- Skrutskie, M. F., Cutri, R. M., Stiening, R., et al. 2003, 2MASS All-Sky Point Source Catalog, IPAC, doi:10.26131/IRSA2
- Stauffer, J., Rebull, L., Bouvier, J., et al. 2016, *AJ*, **152**, 115
- Stauffer, J., Collier Cameron, A., Jardine, M., et al. 2017, *AJ*, **153**, 152
- Stauffer, J., Rebull, L., David, T. J., et al. 2018a, *AJ*, **155**, 63
- Stauffer, J., Rebull, L. M., Cody, A. M., et al. 2018b, *AJ*, **156**, 275
- Stauffer, J., Rebull, L. M., & Jardine, M. 2021, *AJ*, **161**, 60
- Stassun, K. G., Oelkers, R. J., Pepper, J., et al. 2018, *AJ*, **156**, 102
- Stassun, K. G., Oelkers, R. J., Paegert, M., et al. 2019, *AJ*, **158**, 138
- Strassmeier, K. G., Rice, J. B., Ritter, A., et al. 2005, *A&A*, **440**, 1105
- Tajiri, T., Kawahara, H., Aizawa, M., et al. 2020, *ApJS*, **251**, 18
- unWISE team 2019, unWISE catalog, IRSA, doi:10.26131/IRSA525
- Werner, M. W., Roellig, T. L., Low, F. J., et al. 2004, *ApJS*, **154**, 1
- Wichmann, R., Bouvier, J., Allain, S., et al. 1998, *A&A*, **330**, 521
- Wright, E. L., Eisenhardt, P. R. M., Mainzer, A. K., et al. 2010a, *AJ*, **140**, 1868
- Wright, E. L., Eisenhardt, P. R. M., Mainzer, A. K., et al. 2010b, AllWISE Source Catalog, doi:10.26131/IRSA1
- Wright, N. J., & Mamajek, E. E. 2018, *MNRAS*, **476**, 381
- Zacharias, N., Monet, D. G., Levine, S. E., et al. 2004, *BAAS*, **36**, 1418
- Zari, E., Hashemi, H., Brown, A. G. A., et al. 2018, *A&A*, **620**, A172
- Zhan, Z., Günther, M. N., Rappaport, S., et al. 2019, *ApJ*, **876**, 127
- Zúñiga-Fernández, S., Bayo, A., Elliott, P., et al. 2021, *A&A*, **645**, A30